Journal of Building Engineering 119 (2026) 115334

Contents lists available at ScienceDirect

Journal of Building Engineering

journal homepage: www.elsevier.com/locate/jobe

Full length article

Data-driven assessment and design recommendations for piloti-type RC buildings based on machine learning techniques

Quoc Bao To [a], Gayoon Lee [a], Jiuk Shin [b], L. Minh Dang [c], Sang Whan Han [d], Kihak Lee [a,*]

[a] *Deep Learning Arctecture Research Center, Department of Architectural Engineering, Sejong University, 209 Neungdong-ro, Gwangjin-gu, Seoul 05006, Republic of Korea*
[b] *Department of Architectural Engineering, Gyeongsang National University, Jinju 52828, Republic of Korea*
[c] *Department of Information and Communication Engineering and Convergence Engineering for Intelligent Drone, Sejong University, 209 Neungdong-ro, Gwangjin-gu, Seoul 05006, Republic of Korea*
[d] *Department of Architectural Engineering, Hanyang University, Seoul 04763, Republic of Korea*

ARTICLE INFO

Keywords:
Piloti structures
Seismic performance prediction
Section shape ratio
Machine learning
Performance-based seismic design

ABSTRACT

This study aims to evaluate the seismic performance of piloti-type reinforced concrete (RC) buildings and to develop an intelligent framework for predicting inter-story drift ratio (IDR) using machine learning techniques. A dataset comprising 111 structural configurations from South Korean piloti structures was analyzed based on key input parameters, including column number (CN), column shape ratio (CSR), wall shape ratio (WSR), concrete compressive strength (f_c'), and transverse spacing (TS). Two machine learning models-Support Vector Machine (SVM) and Adaptive Neuro-Fuzzy Inference System (ANFIS) were developed and compared. Among the models, ANFIS demonstrated superior accuracy, with R^2 values exceeding 0.95 and error metrics (MAE, MSE, $RMSE$) within acceptable limits. The model's predictions were further validated through finite element (FE) analysis using LS-DYNA pushover simulations. The predicted IDR values closely matched the FE results, with discrepancies below 10%. Parametric analysis confirmed that optimal seismic performance was achieved when CSR ranged from 1.0 to 1.5 and WSR from 1.5 to 2.78. Based on these findings, design recommendations were proposed for both new construction and retrofit applications, tailored to moderate and high seismic hazard zones.

1. Introduction

1.1. Background

Recent catastrophic earthquakes have severely impacted numerous seismically vulnerable reinforced concrete (RC) structures, resulting in substantial loss of life and significant economic damage. For instance, the 2011 Tōhoku earthquake in Japan caused the complete destruction of over 120,000 buildings, with hundreds of thousands more partially or moderately damaged. More recently, the 2023 Kahramanmaraş earthquakes in Turkey led to the collapse or severe damage of over 60,000 buildings, exposing widespread deficiencies in older RC structures and emphasizing the urgent need for seismic resilience.

---

* Corresponding author.
E-mail addresses: baoquocbk2012@gmail.com (Q.B. To), kihaklee@sejong.ac.kr (K. Lee).

https://doi.org/10.1016/j.jobe.2026.115334
Received 8 April 2025; Received in revised form 29 December 2025; Accepted 17 January 2026

Table 1
The performance levels regarding both structural and non-structural.

Level	Seismic performance	Characteristics
1	Operational (OP)	- The building is readily appropriate for standard usage with negligible or no damage to the structural and non-structural elements.
2	Immediate occupancy (IO)	- The structure sustains negligible or no damage to the structural elements and relatively modest damage to the non-structural components. - Immediate occupancy could be feasible. Nevertheless, certain clean-up, repair, and restoration of service utilities may be required prior to the building resuming its pre-earthquake functionality.
3	Life safety (LS)	- The structural and non-structural elements have sustained significant damage and require repairs prior to re-occupancy. Repair is feasible but may be economically unviable.
4	Collapse prevention (CP)	- The structural failure is averted without regard for non-structural weaknesses. The structure may pose a substantial risk to life safety and be regarded as a total economic loss.

In seismically active regions, modern buildings are typically designed in accordance with strict safety and performance standards outlined in contemporary building codes. However, a large portion of the existing building stock-particularly those constructed prior to the implementation of these codes-remains highly susceptible to seismic damage. In this context, retrofitting and strengthening existing RC structures have emerged as cost-effective and practical solutions to enhance structural performance and mitigate future losses [1–4].

Piloti-type reinforced concrete (RC) buildings have sustained substantial damage in recent earthquakes due to their inherent structural vulnerabilities. These buildings typically consist of two distinct structural systems: (1) a moment-resisting frame at the ground level, often used for parking spaces, and (2) a shear wall system supporting the residential units on the upper stories. In densely populated urban regions, the scarcity of land has led to the widespread adoption of this architectural configuration. In particular, three-to six-story buildings featuring a piloti story at the ground level are common in cities across Korea and China, especially in mixed-use and residential developments [5–7].

Despite their prevalence, piloti-type structures have been inadequately addressed in many building codes, lacking explicit design provisions for their unique hybrid system. As a result, these buildings are often engineered to resist the upper-story shear wall loads while employing relatively flexible and lightly reinforced frames at the ground level. This stiffness–strength mismatch concentrates lateral deformation in the first story, leading to soft-story failure, which have been observed in numerous past earthquakes [8–10].

Most regional and international building codes provide limited guidance regarding the expected performance of structures following seismic events. In response, an international trend has emerged toward the development of performance-based seismic design frameworks, which aim to deliver a clear, quantifiable characterization of structural behavior under future earthquakes. Performance-based earthquake engineering encompasses the design, assessment, and construction of structures to meet the seismic performance expectations of stakeholders, including owners, users, and regulatory authorities [11–15].

This approach requires the ability to reliably predict structural performance, thereby enabling engineers and clients to select desired performance levels under different levels of seismic intensity. Such decisions influence both the design philosophy and the associated construction costs. Factors such as building importance, intended lifespan, and acceptable risk are typically considered in selecting performance targets. The performance level represents the maximum allowable extent of damage a structure can sustain during a specified design-level earthquake.

FEMA 273 (1997) and FEMA 356 (2000) [16,17] formalized this concept by defining structural and non-structural performance objectives across multiple levels. These performance levels-including Operational, Immediate Occupancy, Life Safety, and Collapse Prevention—are summarized in Table 1.

In recent years, machine learning (ML) techniques have been increasingly applied to solve complex problems in structural engineering. These data-driven methods provide an efficient alternative to conventional approaches that rely heavily on time-consuming numerical simulations and expensive experimental campaigns. ML models have demonstrated strong capabilities in capturing nonlinear structural behavior and identifying key patterns in large datasets [18–20].

In particular, ML has been employed to evaluate the seismic performance of reinforced concrete (RC) columns retrofitted with fiber-reinforced polymer (FRP) composites, and to predict the nonlinear response of RC structures under earthquake excitation [21]. These applications highlight the potential of ML frameworks to support structural assessment, damage forecasting, and performance-based design with enhanced speed and accuracy.

1.2. Research purpose

This study aims to investigate the influence of section shape ratios and to develop robust ML models for predicting the seismic performance of piloti-type reinforced concrete (RC) buildings in South Korea. The evaluation framework begins with the estimation of seismic demands and damage states, incorporating drift-based performance criteria to assess structural response.

To examine the effect of CSR on seismic behavior, experimental tests were conducted on two full-scale RC specimens with different column cross-sections, referred to as Specimen 1 and Specimen 2, under cyclic lateral loading. Following the experimental phase, several ML models were constructed and evaluated to predict seismic damage levels. The model selection process was based

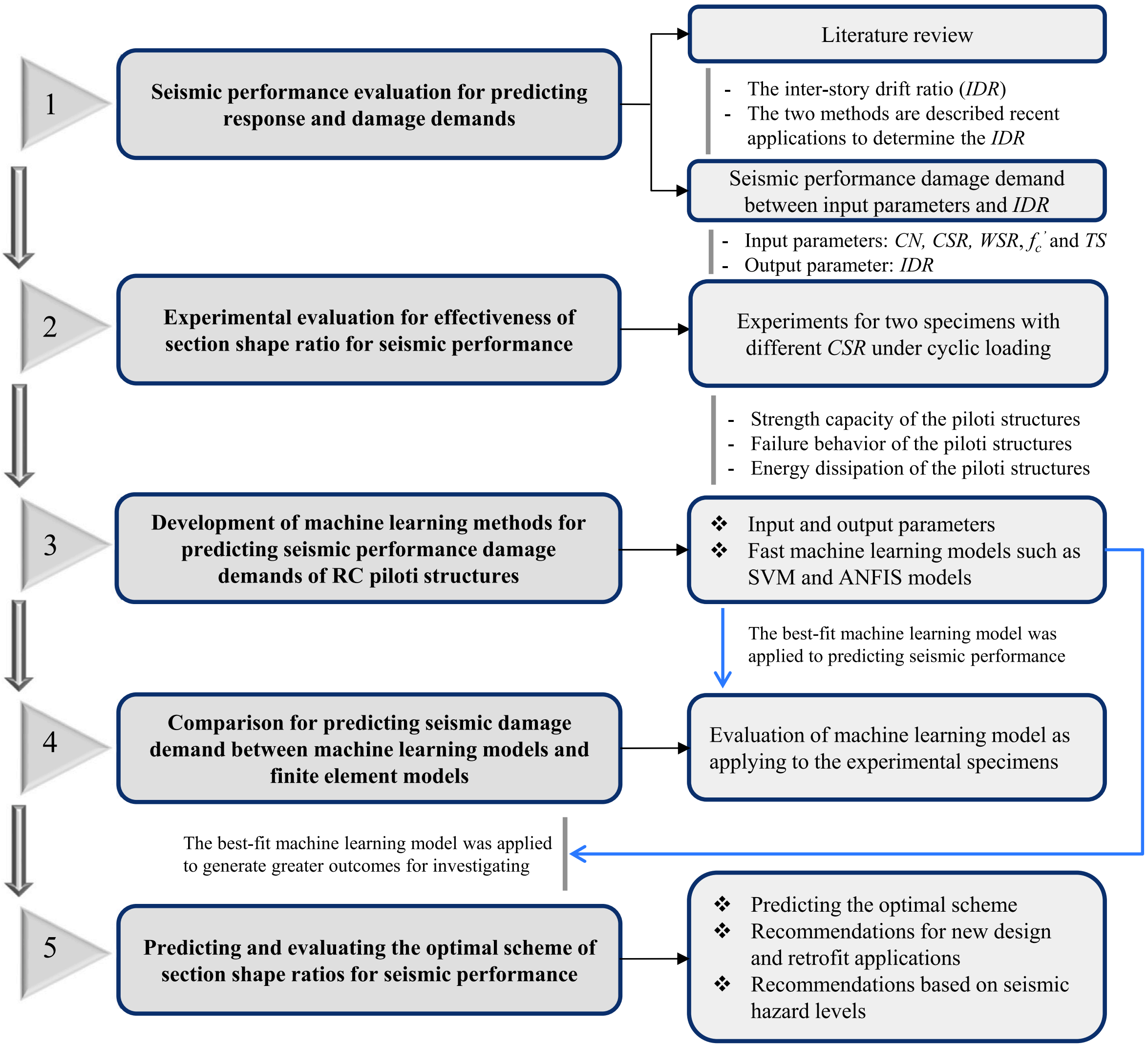

Fig. 1. Methodology flowchart for this study.

on standard performance metrics, including the coefficient of determination (R^2), mean absolute error (MAE), mean squared error (MSE), and root mean squared error ($RMSE$).

The most accurate model was subsequently utilized to simulate seismic performance under a range of section shape ratio configurations, leading to the identification of optimal design recommendations for both new construction and retrofit scenarios. The overall research methodology is schematically illustrated in Fig. 1.

2. Seismic performance evaluation for predicting response and damage demands based on the IDR

2.1. Literature review

The IDR refers to the proportion of the relative translational displacement between two successive floors and the height of the story. This statistic holds significant importance in assessing the structural integrity of structures subjected to seismic loads. The two methods are described recent applications to determine the IDR, which are classified as either contact or non-contact.

Contact method is presumably, the most straightforward way to obtain IDR is to directly measure the absolute displacement of each floor using a displacement sensor such as a linear variable differential transformer (LVDT). This, however, requires a rigid reference frame which is impractical for field deployments. The next logical step is to directly measure relative displacements (floor-to-floor) which can be done with an LVDT, and a spring tensioned wire diagonally strung across a bay. This approach works reasonably well in laboratory set-ups at moderate scales, where results can be verified with external reference displacements [22].

Table 2
Code-defined drift limits for different performance levels in FEMA 356 [17].

Level (i)	Seismic performance level (PL_{Si})	Drift limit (IDR)
1	PL_{S1} — Operational (OP)	≤0.5%
2	PL_{S2} — Immediate occupancy (IO)	≤1.0%
3	PL_{S3} — Life safety (LS)	≤2.0%
4	PL_{S4} — Collapse prevention (CP)	≤4.0%

However, it is less effective for actual buildings where the wire spans long distances and becomes susceptible to sagging [23]. Finally, this approach is impractical for deployment in buildings with occupants and typically numerous partition walls.

Non-contact is current GPS technology that can sample at 20 Hz within a translational accuracy of ±1 cm and has been successfully used to monitor roof displacements of tall buildings [24–26] and other long-period structures. Although its deployment is limited primarily to roof installations, this system offers several advantages. One immediate obvious advantage is in the ease and unobtrusiveness of deployment. GPS sensors could also be used to verify displacements obtained by nearby accelerometers. Difficulties associated here include non-ideal locations with potential variations in ground motions as compared to the building site.

According to the PIP STC01015 structural design criteria [27], the allowable IDR for occupied structures is limited to $1/200$. In contrast, the technical specification for concrete structures of tall buildings in China (JGJ3-2010) [28] stipulates a more stringent limit of $1/550$ for frame structures. These drift limitations are intended to: (1) prevent stress fractures or damage in vertical load-bearing components, thereby preserving structural integrity; (2) protect non-structural elements from excessive deformation, ensuring the continued serviceability of the structure; and (3) maintain the overall stability of the building under lateral loading.

The IDR comprises two components: a detrimental portion caused by the deformation of vertical elements, which can lead to direct stress and potential damage; and a non-detrimental portion resulting from the rigid-body rotation of the lower story, which does not significantly affect structural safety [29]. Of these, the detrimental IDR serves as a more direct indicator of stress within structural components.

2.2. *Seismic performance evaluation for predicting response and damage demands*

The dataset used in this study consists of 111 cases derived from actual piloti-type reinforced concrete buildings in Korea, collected based on available design documents and reported structural information. The selected buildings represent typical low- to mid-rise residential piloti configurations commonly adopted in practice. To ensure consistency in seismic performance evaluation and to isolate the effects of key geometric parameters, the investigated cases were limited to plan-regular structural systems. Potential plan or vertical irregularities that may induce significant torsional seismic responses were not explicitly considered in this study. Accordingly, torsional effects are beyond the scope of the present work and are identified as an important topic for future investigation, as detailed in Appendix.

Structural performance levels are commonly evaluated using the IDR values, which were obtained through analytical evaluation of piloti-type RC buildings under lateral loading, as listed in Appendix. For each building, structural analyses were conducted independently in the two principal horizontal directions (X- and Y-directions). The IDR was calculated as the ratio of the relative story displacement to the corresponding story height. To represent the seismic deformation demand conservatively, the maximum IDR obtained from the two orthogonal directions was adopted as the representative value for each building, thereby implicitly accounting for unfavorable alignment between the seismic excitation direction and the strong or weak axes of vertical structural elements. This procedure is consistent with standard practice in seismic performance assessment and ensures that the most critical directional response is captured.

Establishing a standardized correlation between observed IDR values and corresponding performance levels remains a complex and ongoing challenge. To address this, FEMA 356 [17] outlines three principal performance levels that define the expected condition of a structure following a seismic event: Operational (OP), Immediate Occupancy (IO), Life Safety (LS), and Collapse Prevention (CP). Each level corresponds to a range of acceptable IDR, varying based on structural system types. These benchmark values are summarized in Table 2.

These classifications serve as essential guidelines for performance-based seismic design and assessment. However, due to variations in material properties, construction quality, and building configurations especially in non-standard forms such as piloti structures the applicability of FEMA's limits may require further verification through empirical or data-driven approaches.

The seismic performance of piloti-type RC buildings in this study is evaluated using five key parameters: CN, CSR, WSR, $f_c{}'$, and TS. The shape ratios of structural sections are characterized by CSR for columns and WSR for walls, as illustrated in Fig. 2. To examine the influence of these parameters on seismic behavior, the correlations between IDR and the selected variables (CN, CSR, WSR, $f_c{}'$, and TS) are presented in Fig. 3. The corresponding dataset is summarized in Appendix.

The piloti-type reinforced concrete structures demonstrated favorable seismic performance across the operational and immediate occupancy performance levels. Specifically, under variations in CN from 2 to 18, $f_c{}'$ from 14.86 MPa to 27.6 MPa, and CSR from 1.0 to 3.43, approximately 80% of the analyzed cases were classified within the operational level, while the remaining 20% fell into the immediate occupancy category.

A wide variation in performance levels was observed with respect to WSR. At WSR values of 2.0, 2.78, and 3.33, the proportion of structures achieving operational-level performance was 90%, 80%, and 60%, respectively. In parallel, the share of cases at the

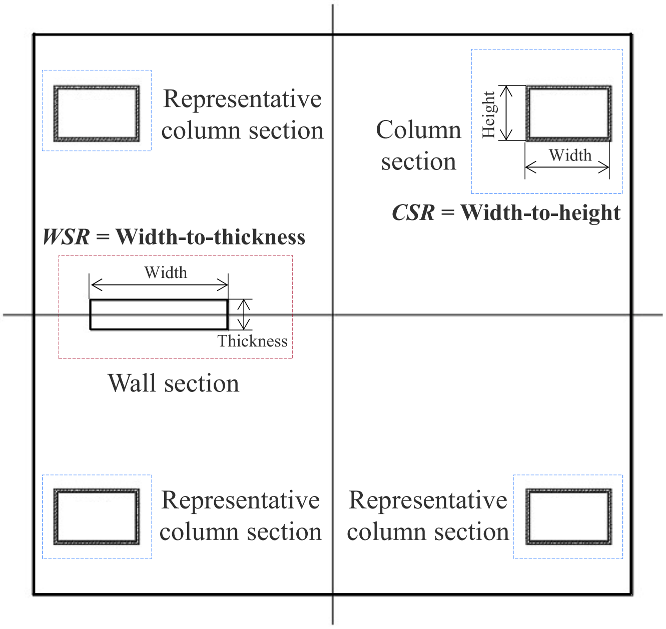

Fig. 2. Definition of column and wall section shape ratios (CSR and WSR).

immediate occupancy level increased correspondingly to 10%, 20%, and 40%. These results indicate that as WSR decreases, the seismic performance of piloti structures improves, reflecting enhanced lateral stiffness and reduced deformation demands.

A similar trend was noted for transverse spacing (TS). Operational-level performance was achieved in 90%, 85%, and 60% of cases at TS values of 200 mm, 250 mm, and 300 mm, respectively. These findings, summarized in Fig. 3, highlight the influence of geometric and material parameters on seismic resilience, emphasizing the importance of optimal section proportioning and spacing in design practice.

2.3. *Experimental evaluation for effectiveness of section shape ratio for seismic performance*

Two piloti-type reinforced concrete specimens were designed and tested to investigate the effect of column section geometry on seismic performance, herein referred to as Specimen 1 (rectangular column) and Specimen 2 (square column) as shown in Fig. 4. Specimen 1 was constructed with a rectangular column section of 250 × 400 mm, while Specimen 2 adopted a square column section of 300 × 300 mm to modify the CSR. Both specimens employed wall sections measuring 150 × 700 mm and were designed with a uniform clear concrete cover of 30 mm. The column longitudinal reinforcement consisted of eight D16 bars, whereas the wall reinforcement comprised twelve D10 bars. Transverse reinforcement was provided using closed stirrups. For the columns, D6 stirrups with a spacing of 300 mm were used for both specimens. For the walls, D10 stirrups with spacings of 250 mm were adopted. Aramid fiber-reinforced polymer (AFRP) sheets were applied only to ensure stable and ductile behavior of the test specimens during cyclic loading and were not treated as a primary study parameter.

To examine the influence of column section geometry on the seismic behavior of piloti-type reinforced concrete structures, two specimens designated as Specimen 1 and Specimen 2 were designed with different CSR.

- Specimen 1 features a rectangular column section with a width-to-height ratio of 1:1.6, representing a slender configuration commonly found in practice to accommodate architectural constraints.
- Specimen 2, by contrast, is configured with a 1:1 square column section, serving as a control specimen to evaluate the effects of aspect ratio variation.

Both specimens were designed with identical material properties, longitudinal and transverse reinforcement detailing, and story height to ensure a direct comparison of shape influence. The mechanical properties of concrete and steel reinforcement are summarized in Table 3. All specimens were cast using ready-mixed concrete with an average compressive strength of 27 MPa. Deformed steel reinforcement with a nominal tensile strength of 450 MPa and a Young's modulus of 200 GPa was used for both longitudinal and transverse reinforcement. These material properties were kept identical for both specimens to ensure that the observed differences in seismic response were primarily attributed to geometric effects.

Lateral cyclic loading was applied under displacement control at the column top to simulate earthquake-induced deformation demands. The boundary conditions were configured to emulate a cantilever column fixed at the base. No external axial load was

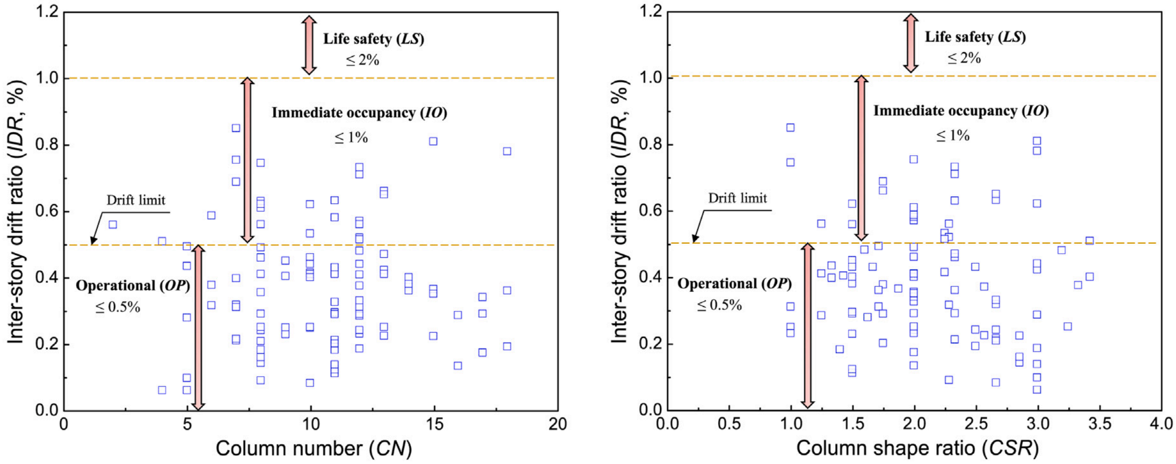

(a) CN-IDR relationship (b) CSR-IDR

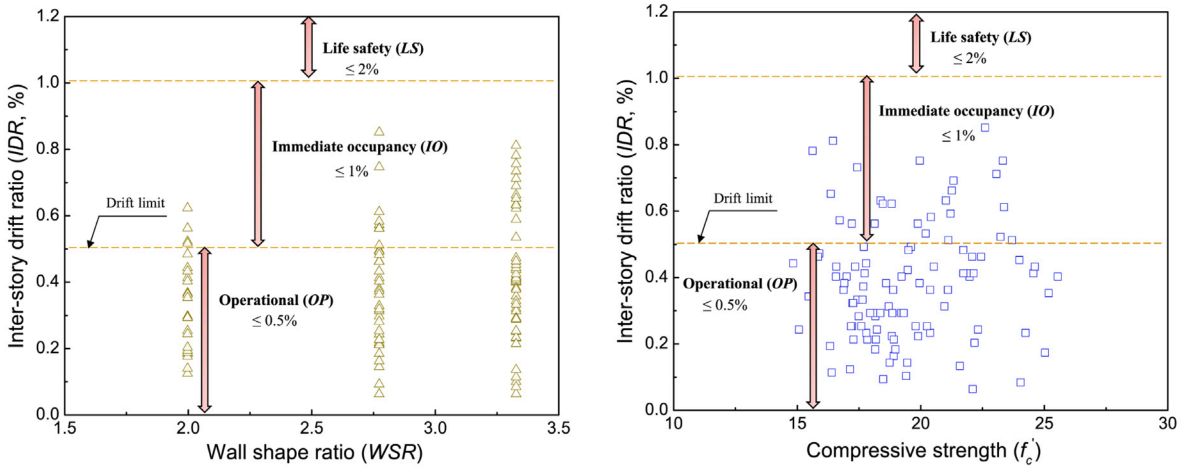

(c) WSR-IDR (d) $f_c{}'$-IDR

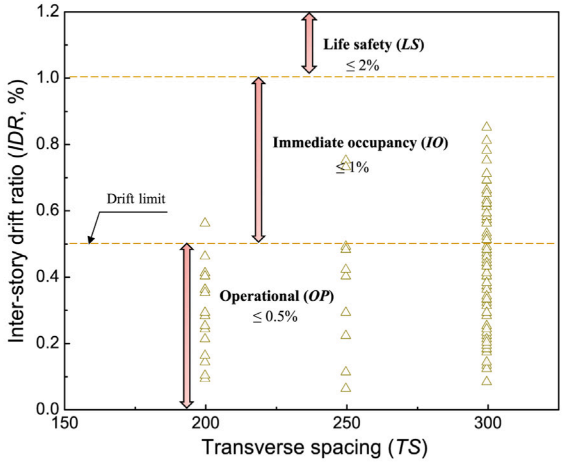

(e) TS-IDR

Fig. 3. Seismic performance damage demand between input parameters and IDR.

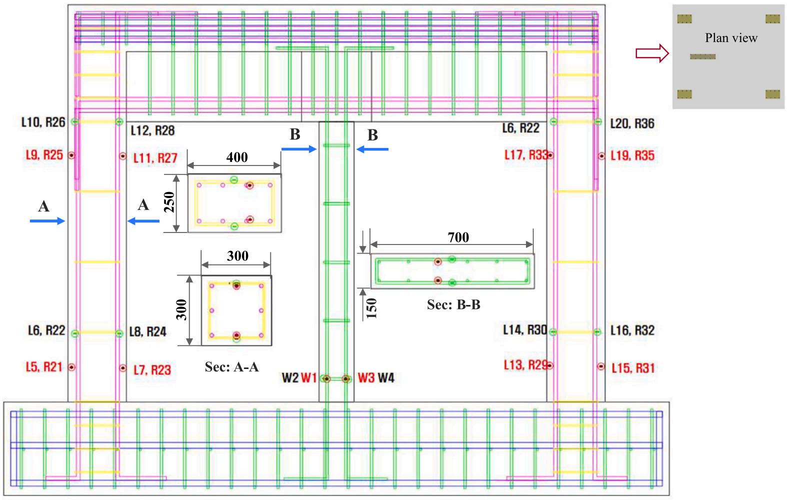

(a) Side view

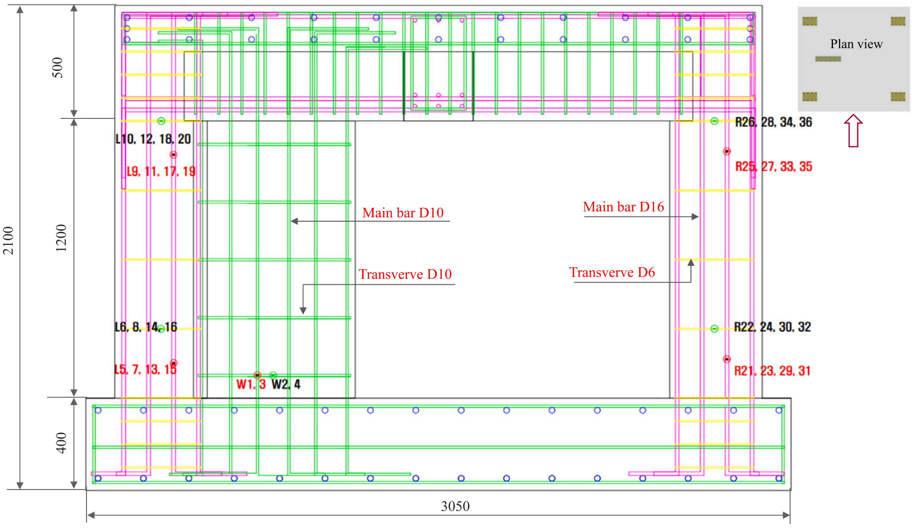

(b) In front of view

Fig. 4. The specimens' designs and strain gauges attachment diagram.

Table 3
Concrete and steel reinforcement mechanical properties.

Mechanical properties	Concrete compressive strength (MPa)	Steel reinforcement	
		Tensile strength (MPa)	Young's modulus (MPa)
Average design value	27	450	200,000

applied during the experiments in order to isolate the influence of column section geometry on the lateral response. Lateral loading was applied independently along the two principal horizontal directions corresponding to the principal axes of the column sections, and the governing response was used for interpretation. Instrumentation included LVDTs to measure displacement and strain gauges on reinforcement to capture internal forces, as shown in Fig. 5.

Fig. 6 illustrates the lateral load–displacement relationships of the two reinforced concrete specimens Specimen 1 and Specimen 2 featuring CSR of 1:1.6 and 1:1, respectively. Both specimens exhibited initial yielding within the IDR range of approximately 0.7% to 0.9%. The maximum lateral strengths were observed at drift ratios of approximately 2.41% for Specimen 1 and 3.53% for Specimen 2.

Fig. 5. Installations and test setup of the piloti structures.

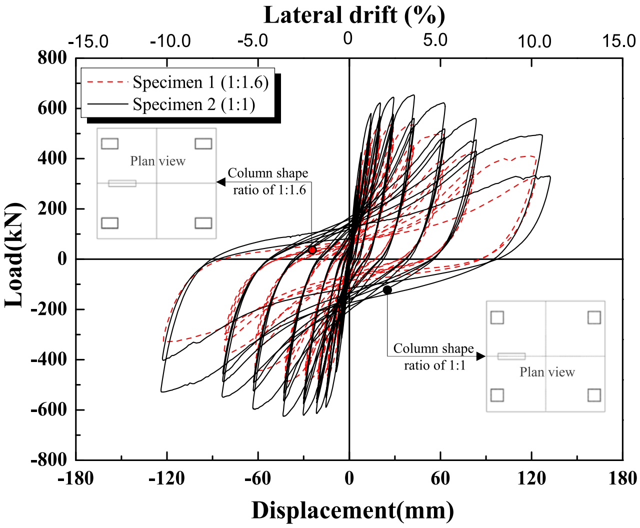

Fig. 6. Effectiveness of the CSR for the strength capacity of the piloti structures.

Following peak strength, both specimens experienced gradual strength degradation and ultimately fractured at large drift ratios of 11.19% and 11.01%, respectively. Specimen 1 achieved a peak load capacity of 541.1 kN in the positive direction and 515.9 kN in the negative direction. In contrast, Specimen 2 recorded peak strengths of 653.6 kN (positive) and 625.4 kN (negative), corresponding to increases of approximately 20.79% and 21.22% over Specimen 1, respectively.

These results indicate that the square column section of Specimen 2 contributed to improved lateral strength capacity and deformation tolerance compared to the more slender rectangular section used in Specimen 1.

Fig. 7 presents the damage progression of the two specimens at various stages of lateral displacement. Visible deterioration began at displacement Step 7 (5.0% drift), where cracks gradually widened, leading to the onset of surface spalling in the concrete columns. By Step 8 (6.67% drift), the crack widths had further increased, resulting in significant spalling and the exposure of longitudinal reinforcement. At this stage, the structural integrity of the column was severely compromised. The failure modes of Specimen 1 and Specimen 2 exhibited distinct characteristics, primarily attributable to the differences in their column section geometries.

Specimen 1, with a rectangular cross-section (shape ratio 1:1.6), exhibited a dominant failure along its weaker axis. Cracking initiated at the column ends and rapidly propagated under increasing drift levels. As lateral displacement progressed, flexural cracks widened, leading to significant spalling of the concrete cover. By 6.67% drift, extensive surface damage was observed, and reinforcement bars were exposed. The asymmetrical shape of the column resulted in reduced lateral stiffness in the weak direction, which contributed to earlier degradation of strength and stiffness. Ultimately, the specimen experienced a flexural-shear failure mechanism, characterized by bar buckling and localized crushing near the plastic hinge region.

Specimen 2, constructed with a square column section (shape ratio 1:1), displayed a more ductile behavior. While cracking patterns were similar in early stages, the damage progression was more uniform, and spalling was comparatively limited. The

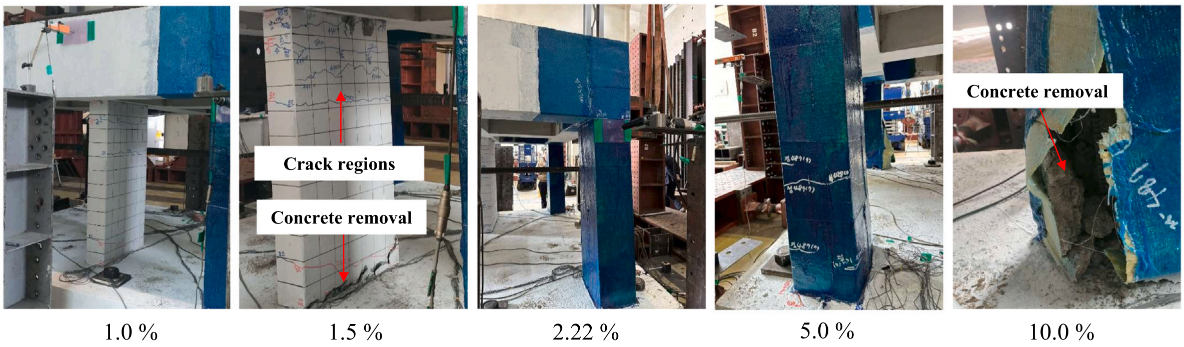

(a) Specimen 1 – $CSR = 1.6$

(b) Specimen 2 – $CSR = 1.0$

Fig. 7. Effectiveness of CSR for failure behavior of piloti structures.

Table 4
Damage progression of Specimen 1 and Specimen 2 at various drift ratios.

Drift ratio (%)	Step	Specimen 1 (Rectangular)	Specimen 2 (Square)
0.7–0.9	Step 3–4	Initial flexural cracks at column base	Initial flexural cracks at column base
2.41 (Peak)	Step 5	Maximum lateral strength reached; crack widening observed	Increased cracking; approaching maximum strength
5.0	Step 7	Surface spalling begins; cracks extend upward	Distributed cracking continues; minor spalling
6.67	Step 8	Severe spalling; reinforcement exposed; concrete cover loss	Spalling initiated; reinforcement partially visible
9.0	Step 9	Functional failure; significant strength degradation; test terminated	Stable residual capacity; no complete failure
11.19 (Ultimate)	Step 10	Fracture of column section; extensive crushing	Progressive damage; maintains integrity

specimen retained higher lateral strength and sustained larger drift ratios with less degradation. The failure mode was predominantly flexural, with distributed cracking and controlled stiffness degradation. No significant signs of premature shear failure or local instability were observed throughout the test.

These findings suggest that the square column section in Specimen 2 provided better confinement and more balanced resistance in both directions, resulting in superior seismic performance. In contrast, the rectangular section of Specimen 1 was more vulnerable to directional weaknesses, leading to earlier and more severe structural damage. Table 4 summarizes the observed damage progression for both specimens at different drift levels.

The energy dissipation behavior of both specimens exhibited a steady increase as the IDR progressed through each loading cycle. In the initial range, up to 0.5% drift, the two specimens demonstrated comparable energy dissipation capacities per cycle. However, at a drift ratio of 1.5%, noticeable fluctuations were observed, indicating divergence in energy absorption performance.

The cumulative energy dissipation values showed a clear difference between the two specimens. Specimen 1 dissipated a total of 43.68 kN m, whereas Specimen 2 reached 60.90 kN m over the full range of applied drift. This corresponds to a 39.42% increase

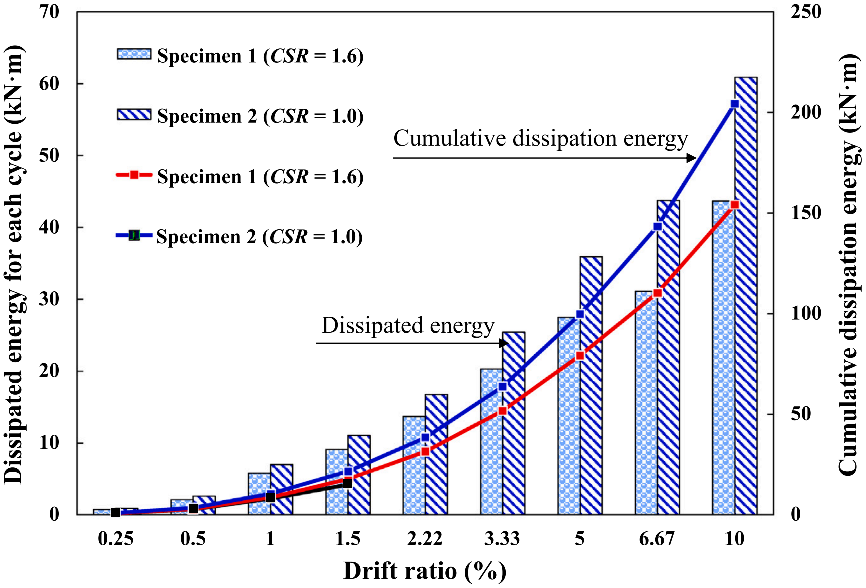

Fig. 8. Effectiveness of the CSR for the energy dissipation of the piloti structures.

in total energy dissipation for Specimen 2, as illustrated in Fig. 8. The superior energy absorption capacity of Specimen 2 can be attributed to its square column cross-section, which provided enhanced symmetry and improved resistance under cyclic lateral loading. These results underscore the importance of CSR in improving the hysteretic behavior and seismic resilience of piloti-type structures.

The experimental results demonstrate the critical influence of column section geometry on the seismic response of piloti-type structures. Despite identical material properties, reinforcement ratios, and boundary conditions, Specimen 2 exhibited higher lateral strength and improved deformation capacity due to its square column section, which provides a more uniform stiffness distribution and enhanced confinement behavior. In contrast, the rectangular section of Specimen 1 led to stiffness imbalance and earlier damage concentration along the weak axis. These observations provide direct physical evidence of the role of column shape ratio in controlling strength, damage progression, and energy dissipation, and support the trends identified through the machine learning predictions and finite element analyses.

3. Development of ML methods for predicting seismic performance damage demands of RC piloti structures

3.1. Input and output parameters

The dataset consists of 111 cases compiled from various piloti-type reinforced concrete structures across South Korea. Each data instance is represented as a five-dimensional real-valued input vector, as detailed in Appendix. The input parameters summarized in Table 5 serve as predictive variables for estimating IDR of piloti structures. These parameters encompass key geometric and material properties relevant to seismic response, and form the basis for developing and training the ML models used in this study. The IDR values considered in this study are intended for relative performance comparison under consistent seismic assessment conditions, rather than for absolute prediction under site-specific ground motion intensities.

- CN: Represents the total number of columns supporting the piloti structure at the ground level. An increased number of columns generally contributes to improved lateral stiffness and reduced drift demand.
- CSR: Defined as the width-to-height ratio of the column cross-section. This geometric proportion significantly influences the flexural and shear behavior of the columns under lateral loads.
- WSR: The ratio of wall width to thickness. Higher WSR values may increase lateral stiffness and resistance; however, excessively large WSR values correspond to thinner wall sections, which can become more vulnerable to shear failure, instability, and unfavorable damage behavior. Consequently, improved seismic performance is observed within an optimal WSR range rather than at extreme values.
- f_c': Denotes the characteristic compressive strength of concrete (in MPa) used in the structure. This material property affects both stiffness and energy dissipation capacity under seismic loading.
- TS: The center-to-center spacing between transverse load-resisting elements (such as columns or walls). Wider spacing may reduce stiffness and increase deformation demand.

Table 5

Summary of input parameters, ranges and training points.

Parameter type	Parameters	Model ranges
Input	Column number (CN)	2.0 to 18
	Column shape ratio (CSR)	1.0 to 3.43
	Wall shape ratio WSR	2.0 to 3.33
	Concrete compressive strength (f'_c)	14.86 to 27.6 MPa
	Transverse spacing (TS)	125 to 400 mm
Output	Inter-story drift ratio (IDR)	–

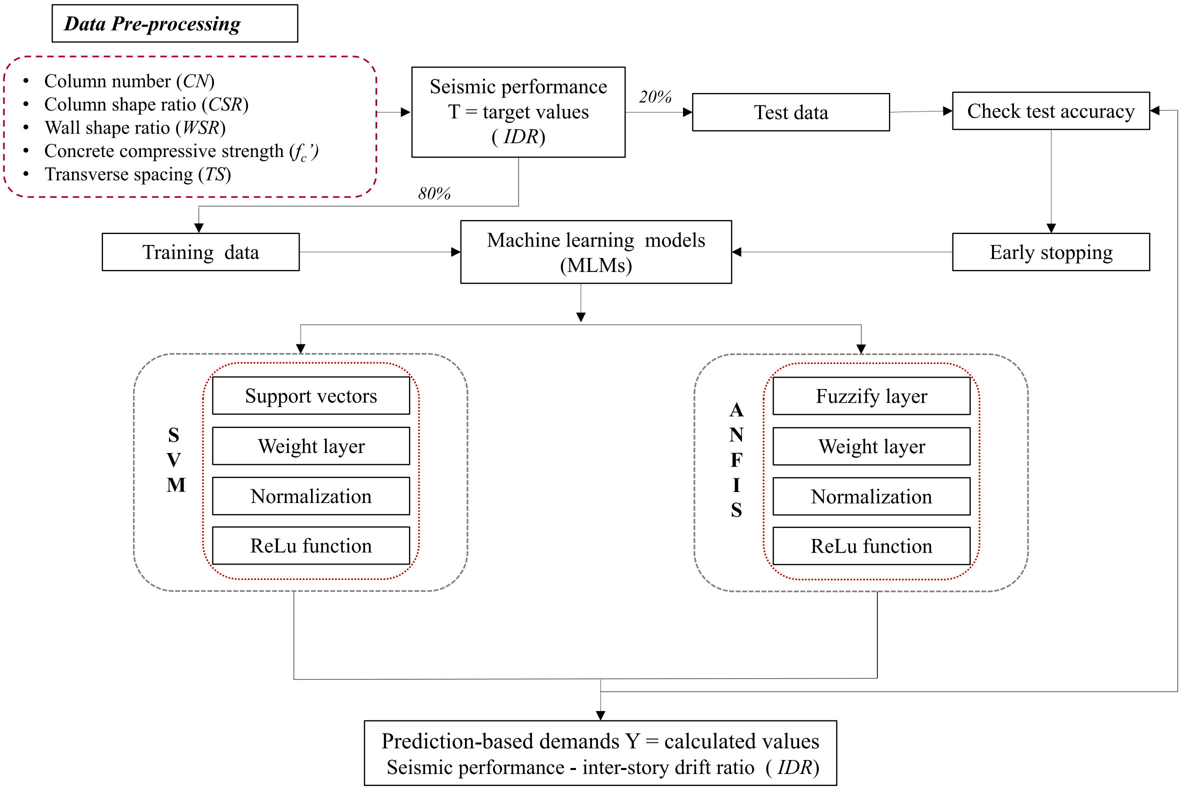

Fig. 9. Flow chart of ML methods to predict seismic performance.

The output variable in this study is IDR, which represents the ratio of relative lateral displacement between two consecutive floors to the height of the story. It is widely regarded as a key engineering demand parameter in performance-based seismic design and evaluation.

The IDR provides direct insight into the deformation demands imposed on structural and non-structural components during seismic events. Excessive inter-story drift is often associated with cracking, damage to infill walls or cladding, and, in severe cases, collapse. As such, many international guidelines including FEMA 356 define performance thresholds based on IDR limits for various structural systems and target performance levels (e.g., Operational, Immediate Occupancy, Life Safety, Collapse Prevention).

In the context of this study, IDR is used not only as a measure of global seismic response but also as the output variable for ML models trained to predict drift demands based on key structural and material parameters. Accurate prediction of IDR enables rapid performance screening of piloti-type reinforced concrete buildings and provides valuable guidance for optimal geometric configurations under seismic loading.

3.2. ML techniques

Two ML algorithms Support Vector Machine (SVM) and Adaptive Neuro-Fuzzy Inference System (ANFIS) were selected for this study due to their unique and complementary strengths, as illustrated in Fig. 9. The SVM model is a non-parametric learning technique that relies on kernel functions to handle high dimensional, non-linear relationships without assuming a specific data distribution. This enables it to perform well in complex regression tasks with limited overfitting.

Table 6
Kernel functions.

Kernel name	Kernel function
Linear	$K(\mathbf{x}_i,\mathbf{x}_j) = \mathbf{x}_i^{\mathrm{T}}\mathbf{x}_j$
Gaussian	$K(\mathbf{x}_i,\mathbf{x}_j) = \exp\left(-\lVert\mathbf{x}_i - \mathbf{x}_j\rVert^2\right)$
Polynomial	$K(\mathbf{x}_i,\mathbf{x}_j) = \left(1+\mathbf{x}_i^{\mathrm{T}}\mathbf{x}_j\right)^q$, where $q \in \{2,3,\dots\}$

In contrast, the ANFIS model integrates the learning capabilities of neural networks with the reasoning structure of fuzzy logic. It provides an adaptive framework capable of modeling highly non-linear systems by continuously updating its membership functions and inference rules based on input–output data. This makes ANFIS particularly effective for capturing subtle patterns in structural behavior under seismic loading.

Both the SVM and ANFIS models were developed and trained using the dataset consisting of 111 cases, with each instance comprising five input features and a corresponding IDR as the output. Prior to training, all input variables were normalized to a range between 0 and 1 to ensure numerical stability and to enhance model convergence.

The dataset was randomly partitioned into two subsets: 80% for training and 20% for testing. Model performance was evaluated using four widely accepted statistical metrics: the coefficient of determination (R^2), root mean square error ($RMSE$), mean absolute error (MAE), and mean squared error (MSE) were calculated using observed and forecasted values in accordance with Eqs. (1)–(3). These metrics collectively assess the accuracy, consistency, and generalization capability of each model.

$$MAE = \frac{1}{N}\sum_{i=1}^{N}\left|Y_i - T_i\right| \tag{1}$$

$$MSE = \frac{1}{N}\sum_{i=1}^{N}(Y_i - T_i)^2 \tag{2}$$

$$RMSE = \sqrt{\frac{1}{(N)\sum_{i=1}^{N}\left(Y_i - T_i\right)^2}} \tag{3}$$

where T is the output of the actual system (measured or observed output), Y is the adaptive intelligent system output and N is the number of instances.

3.2.1. SVM model

In recent decades, there have been substantial advancements in the theoretical comprehension of SVM, alongside algorithmic methodologies for their implementation and applications to practical issues. The SVM, developed by Vapnik and colleagues in the early 1990s, are ML systems that employ a hypothesis space of linear functions within a high-dimensional feature space, trained using optimization algorithms that apply a learning bias based on statistical learning theory [30,31].

SVMs are founded on statistical learning theory and originate from the structural risk reduction principle, aiming to reduce both empirical risk and the confidence interval of the learning model to enhance generalization performance. SVMs have demonstrated exceptional robustness and efficiency as algorithms for classification and regression. The specifics of SVM regression are referenced in Vapnik et al. [32,33]. The main concept of SVM regression is summarized as follows. Consider a training dataset with a multivariate set of N observations, denoted as x_i and x_j, together with the corresponding observed response values Y_n. The decision function of nonlinear support vector regression, incorporating the kernel trick, is articulated as Eq. (4). The dual representation of the nonlinear support vector regression can be articulated as:

$$\mathrm{Min}L(\alpha) = \frac{1}{2}\sum_{i=1}^{N}\sum_{j=1}^{N}\left(\alpha_i - \alpha_i^*\right)\left(\alpha_j - \alpha_j^*\right)K\left(x_i, x_j\right) + \varepsilon\sum_{i=1}^{N}\left(\alpha_i - \alpha_i^*\right) - \sum_{i=1}^{N}Y_i\left(\alpha_i - \alpha_i^*\right) \tag{4}$$

Subject to

$$\sum_{i=1}^{N}\left(\alpha_i - \alpha_i^*\right) = 0$$

$$\forall n : 0 \le \alpha_n \le C$$

$$\forall n : 0 \le \alpha_n^* \le C$$

where constant C is the box constraint, $K\ (x_i,\ x_j)$ is the kernel function. Several types of kernel functions are listed in Table 6.

The decision function of nonlinear SVM, incorporating the kernel trick, is articulated as follows. The structure of the SVM model is illustrated in Fig. 10. Comprehensive theoretical foundations and fundamental SVM formulas are available in numerous sources in Eq. (5), particularly in Refs. [30,34].

$$f(x) = \sum_{n=1}^{N}\left(\alpha_n - \alpha_n^*\right)K\left(x_n, x\right) + b \tag{5}$$

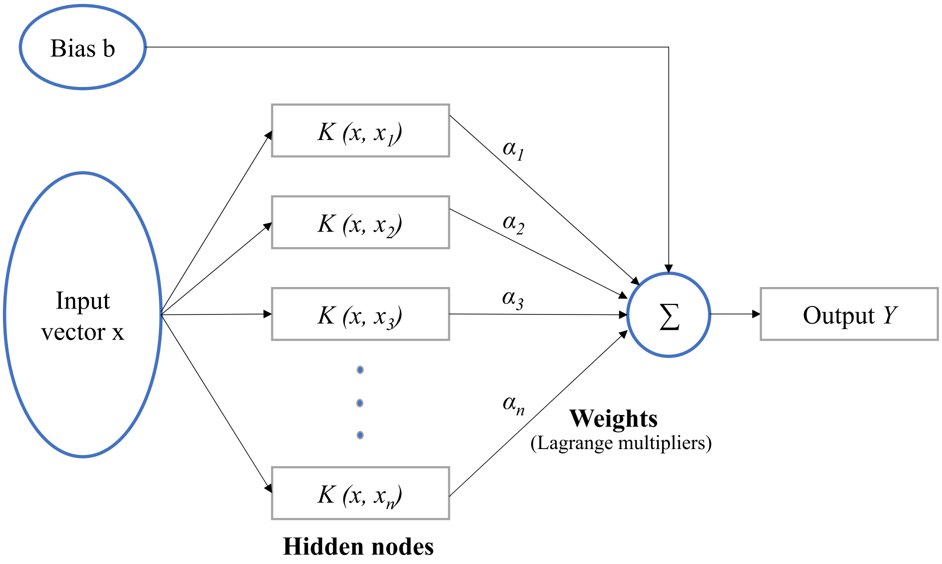

Fig. 10. Structure of SVM model.

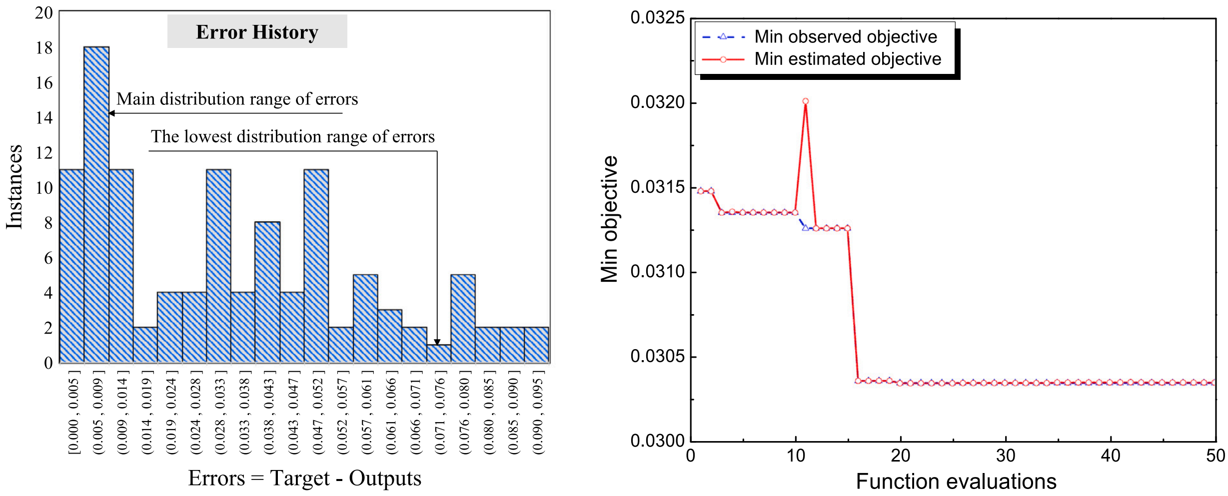

(a) Error histograms

(b) Convergence history

Fig. 11. Performance evaluation for SVM model.

where α_n, α_n^* are non negative multipliers which are the solutions of the optimization problem.

Fig. 11 presents the regression results of the SVM model, trained and tested on a dataset comprising 111 cases of piloti-type structures across South Korea, as detailed in Appendix. The figure includes an error histogram (Fig. 11a), which displays the distribution of prediction errors over 20 bins for both the training and testing sets. The highest concentration of data points is centered around the zero-error point, indicating excellent model accuracy. Notably, approximately 85% of the predictions fall within an error margin of less than 1%, demonstrating the robustness and reliability of the SVM model.

Additionally, the SVM convergence behavior is shown in Fig. 11b, where the predicted IDR values are plotted against the actual values. The model achieved convergence after 17 iterations, with a strong correlation observed between predicted and actual outputs. The minimal spread in the residuals suggests a high level of agreement, confirming the effectiveness of the SVM approach in modeling the non-linear relationship between structural input features and IDR.

The performance of SVM model is depicted in Fig. 12, where eleven randomly selected samples excluded from the training process were used for independent evaluation. These samples, drawn from the dataset presented in the Appendix, served to validate the model's generalization capability. As shown in the figure, the training and testing prediction curves exhibit close agreement, with no significant divergence, indicating the absence of overfitting and a well-generalized model.

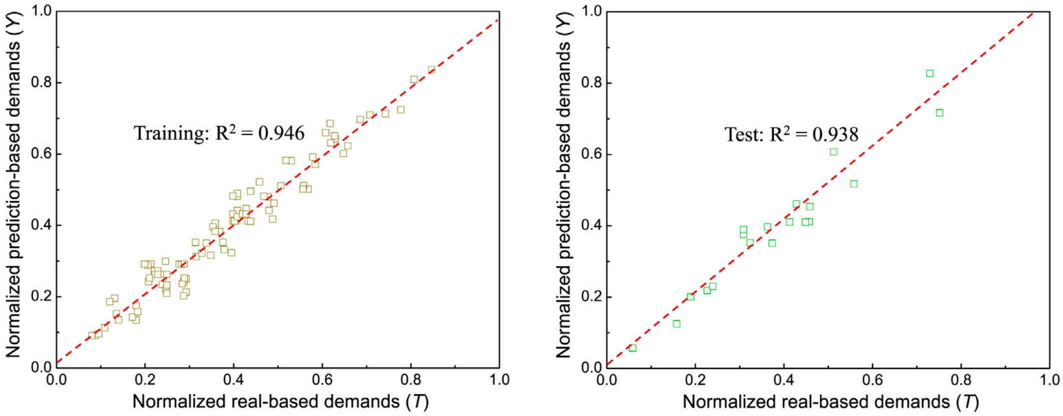

(a) Training (b) Test

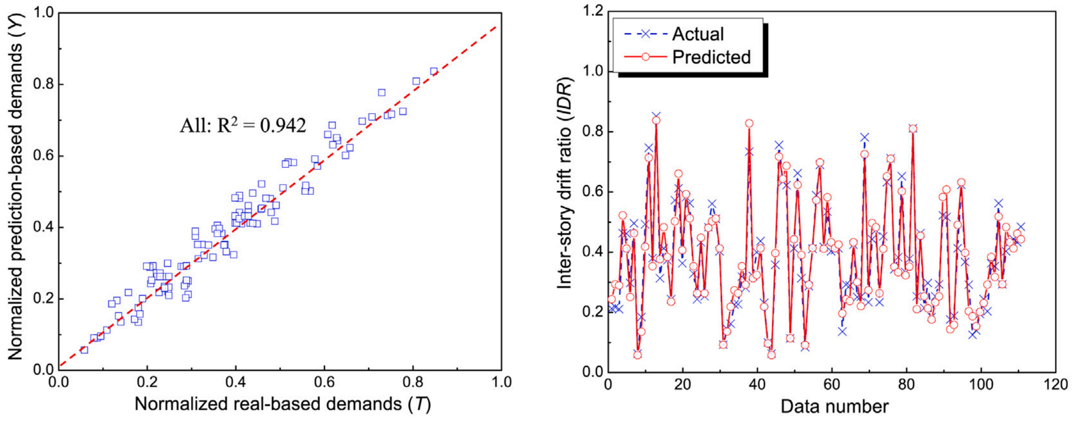

(c) All data (d) Actual and predicted values (All data)

Fig. 12. Performance evaluation — Regression analysis for the SVM simulation.

Table 7
Seismic performance evaluation of the SVM model.

Model	Statistical parameter	Requirements	Calculated results	Remarks
SVM model	MAE	Close to 0	0.022	–
	MSE	Close to 0	0.019	–
	$RMSE$	Close to 0	0.122	–
	R^2	Greater than 0.9	0.942	–

The model's predictive accuracy was quantitatively assessed using several statistical indicators. The coefficient of determination (R^2) values for the training, testing, and overall datasets were 0.946, 0.938, and 0.942, respectively, confirming a strong linear correlation between predicted and actual IDR values across all data subsets.

In addition, MAE, MSE, and $RMSE$ were found to be 0.022, 0.019, and 0.122, respectively. These low error metrics, summarized in Table 7, reinforce the model's reliability and consistency in estimating seismic response. The results demonstrate that the SVM model is capable of capturing complex, non-linear relationships within the structural dataset and can effectively predict higher drift responses under challenging configurations.

3.2.2. ANFIS model

An ANFIS is an advanced artificial intelligence framework that synergistically combines the learning capabilities of artificial neural networks with the interpretability and reasoning power of fuzzy logic systems. ANFIS possesses the ability to learn from data in a manner similar to neural networks, while simultaneously handling uncertainty and imprecision, akin to fuzzy inference systems. This hybrid architecture makes ANFIS particularly suitable for applications involving complex, non-linear, or ambiguous data environments.

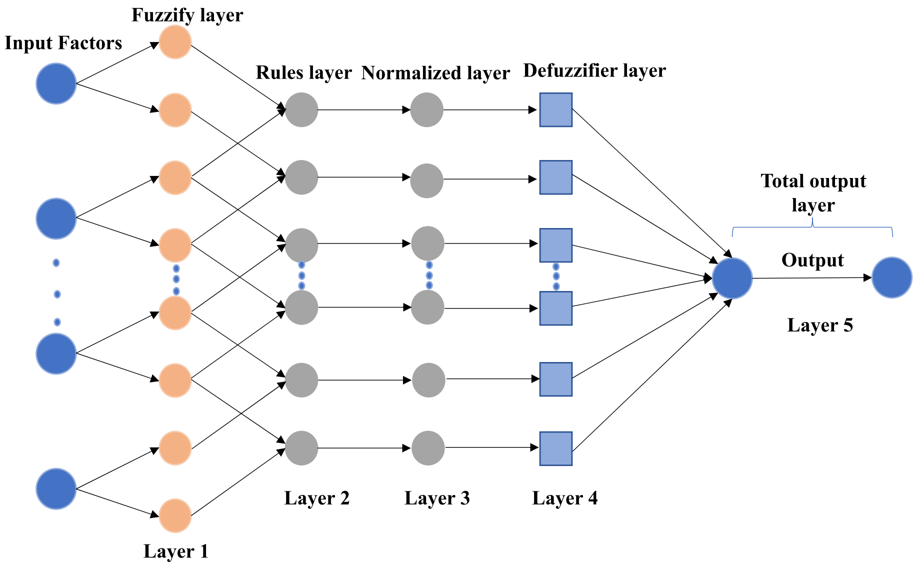

Fig. 13. Structure of ANFIS model.

Structurally, ANFIS operates as a multi-layer feedforward network, where each node performs a specific function and is associated with adjustable parameters. The learning algorithm continuously updates the connection weights between nodes based on training data, thereby enabling the system to adaptively refine its decision-making process.

The standard ANFIS architecture comprises five sequential layers: (1) fuzzification, (2) rule generation, (3) normalization, (4) defuzzification, and (5) output summation, as illustrated in Fig. 13. Within this framework, the Takagi–Sugeno (T–S) fuzzy inference system is widely adopted. Unlike traditional fuzzy models that use fuzzy sets in the output, the T–S model employs weighted linear functions of input variables, enabling more precise and efficient rule-based predictions.

By leveraging both data-driven learning and fuzzy rule-based reasoning, ANFIS can effectively generalize from observed data and forecast outcomes for novel input conditions. This makes it a powerful tool for modeling structural responses in civil engineering applications, particularly when dealing with highly non-linear behavior under seismic loading conditions [35–38].

Fuzzy systems enable the formal representation of human expert knowledge through fuzzy IF–$THEN$ rules, which serve as the foundational units for reasoning and knowledge acquisition within such systems. Similar to traditional rules used in symbolic artificial intelligence, a fuzzy rule consists of two main components: the antecedent (the “IF” clause) and the consequent (the “$THEN$” clause). The general form of a fuzzy rule is expressed in Eq. (6).

Unlike crisp logic, where the antecedent is either true or false, the antecedent in a fuzzy rule is evaluated to a certain degree of truth, typically ranging between 0 and 1. Multiple antecedent conditions can be combined using logical operators such as AND, OR, and NOT, allowing for the construction of more complex rule structures, analogous to conventional Boolean logic. Fuzzy rule consequents can be categorized into two primary types: (1) Fuzzy consequents, in which the output is a fuzzy set defined by a membership function, (2) Functional consequents, commonly used in Takagi–Sugeno (T–S) models, where the output is a crisp function (usually a linear or constant function) of the input variables. These rules form the basis for the fuzzy inference mechanism, allowing systems like ANFIS to model complex and non-linear behavior while maintaining interpretability and adaptability.

$$IF < antecedent > THEN < consequent > \tag{6}$$

The optimal configuration of the proposed ANFIS model was achieved at an influence radius (r) of 0.45, resulting in the generation of 50 fuzzy rules. This parameter setting provided the best trade-off between model complexity and prediction accuracy. The structure of the ANFIS network incorporating these 50 rules each constructed using the logical ‘AND’ operator is depicted in Fig. 14.

Furthermore, Fig. 15 illustrates the specific fuzzy rules activated by a sample input case with the following parameter values: $CN = 10$, $CSR = 2.21$, $WSR = 2.67$, $f_c{}' = 20.2$ MPa, and $TS = 250$ mm. These rules demonstrate the interpretability of the ANFIS model, as it systematically combines input conditions through fuzzy logic to infer an appropriate output response in this case, the predicted IDR.

A parametric analysis was conducted to evaluate the influence of individual input variables on the predicted IDR. To visualize the interactions between input features and the output, three-dimensional surface plots were employed. These plots illustrate the non-linear relationships learned by the ANFIS model and provide insight into the sensitivity of the output to varying input combinations.

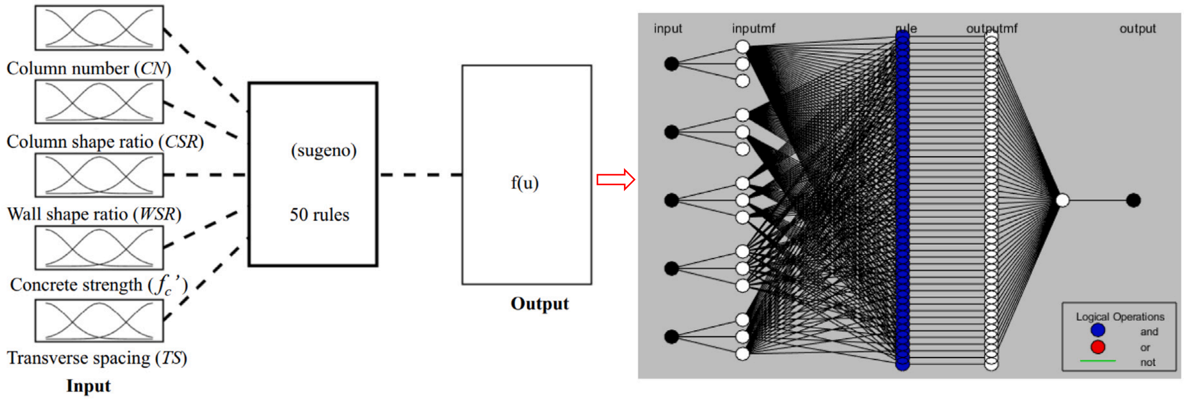

Fig. 14. Structure of ANFIS model by using MATLAB software.

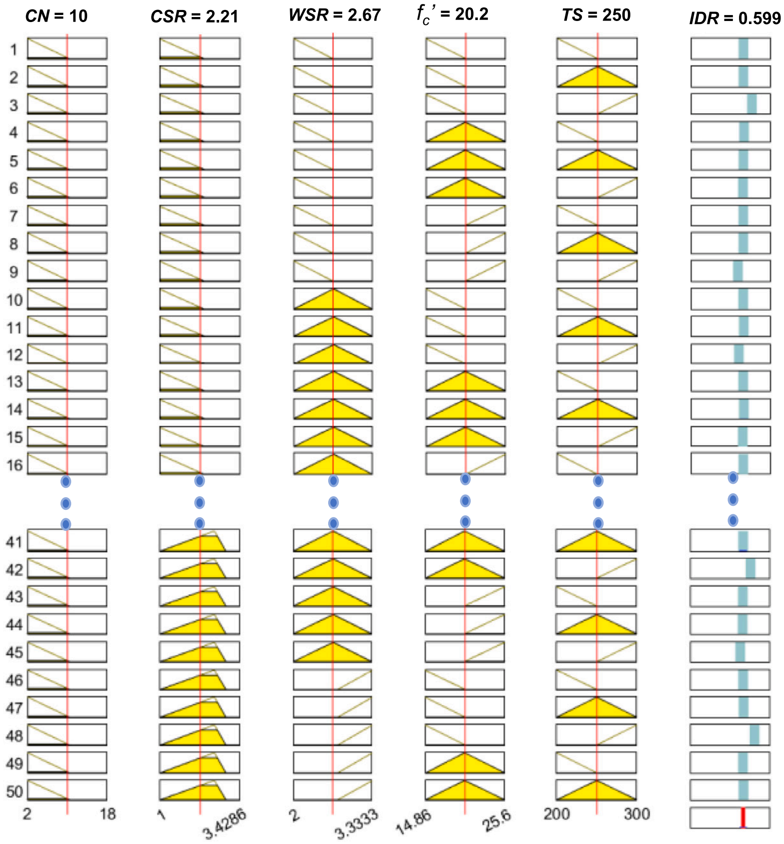

Fig. 15. ANFIS rule structure with 50 rules.

Fig. 16 presents representative surface plots demonstrating the CSR and WSR on the predicted IDR, while holding other parameters constant at representative values: $CN = 10$, $f'_c = 20.2$ MPa, and $TS = 250$ mm. The maximum predicted IDR values were observed around $CSR = 2.21$ and $WSR = 2.67$, indicating a region of elevated deformation demand.

While, in theory, each input parameter may exhibit an independent and continuous relationship with the output, this assumption does not hold within the adaptive neuro-fuzzy framework of ANFIS. Instead, the influence of each input on the output is highly dependent on the combination of other input variables. As a result, the surface plots generated by the ANFIS model display complex patterns of curvature, extrema, and interaction effects, reflecting the dynamic nature of the learned fuzzy rules.

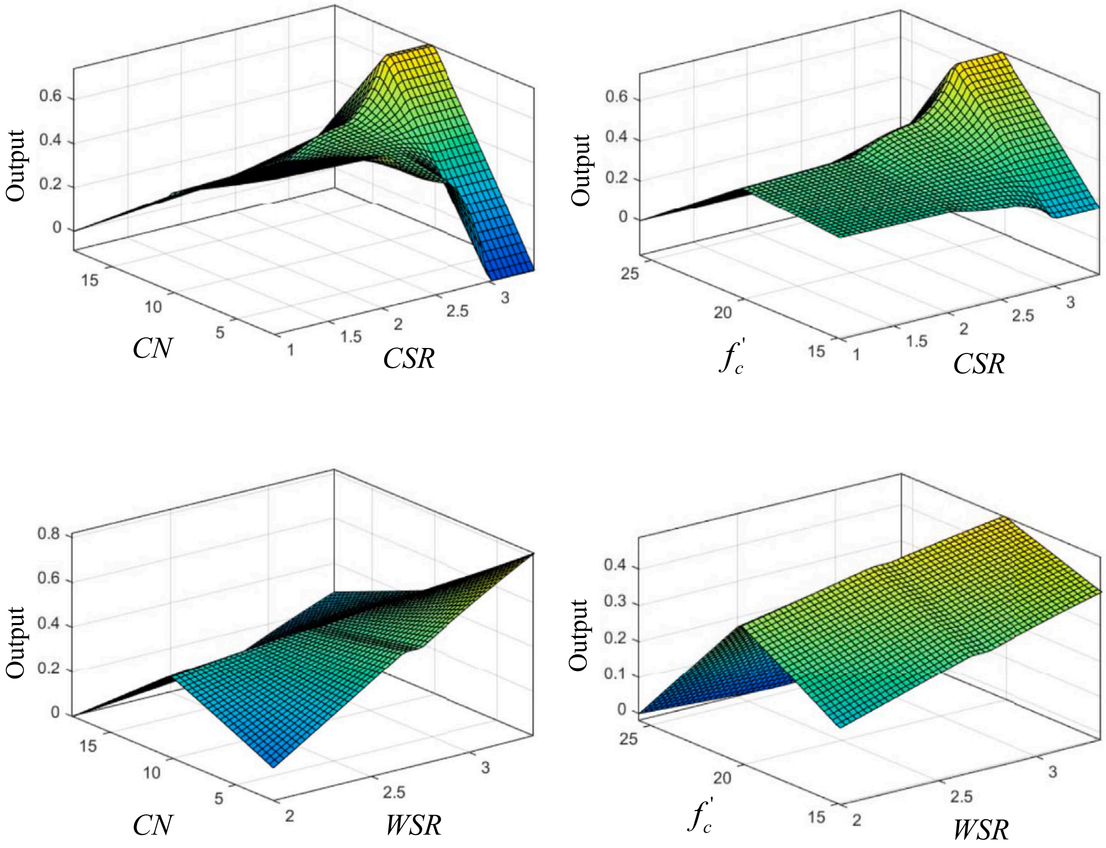

Fig. 16. ANFIS rule structure with 50 rules.

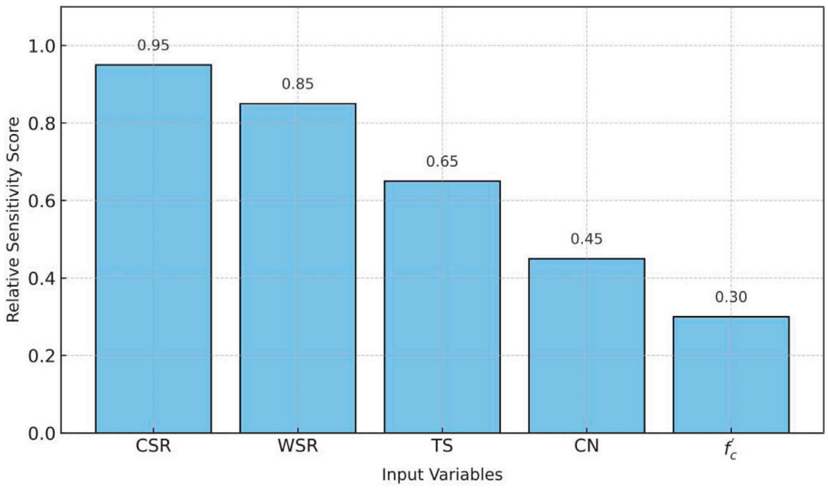

Fig. 17. Sensitivity ranking of input variables on IDR prediction.

The sensitivity ranking was established by evaluating the partial derivative-based influence of each input, as well as observing the curvature and variation of output responses across the range of each variable in the generated surface plots as shown in Fig. 17. The following key observations were made: CSR exhibited the highest sensitivity, indicating that changes in column proportions significantly influence lateral deformation behavior. Additionally, WSR ranked second, showing strong interaction effects with CSR and considerable influence on IDR due to its role in lateral stiffness.

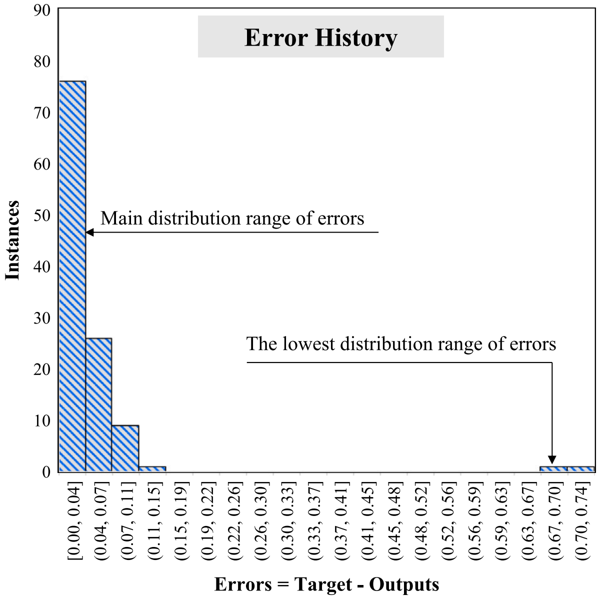

Fig. 18. Performance evaluation for ANFIS model.

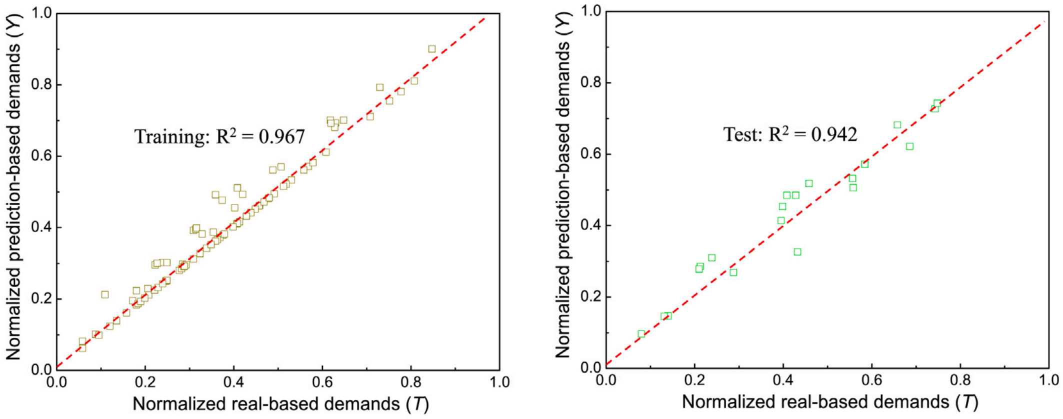

(a) Training (b) Test

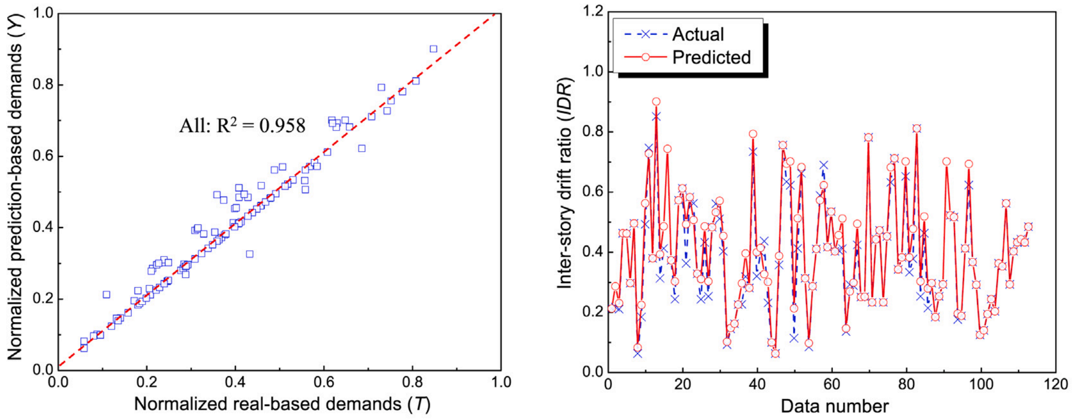

(c) All data (d) Actual and predicted values (All data)

Fig. 19. Performance evaluation — Regression analysis for the ANFIS simulation.

Table 8
Seismic performance evaluation of the ANFIS model.

Models	Statistical parameter	Requirements	Calculated results	Remarks
ANFIS model	MAE	Close to 0	0.172	Best-fit model
	MSE	Close to 0	0.011	Best-fit model
	$RMSE$	Close to 0	0.104	Best-fit model
	R^2	Greater than 0.9	0.958	Best-fit model

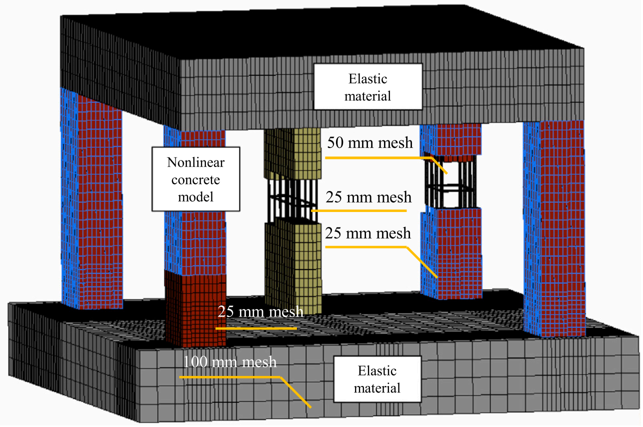

Fig. 20. FE model for RC piloti structures.

Fig. 18 presents the regression results of the ANFIS model, trained and tested using data collected from various piloti-type reinforced concrete structures across South Korea, as detailed in Appendix. The figure includes an error histogram that visualizes the distribution of prediction errors across all data points within the network, using 20 bins.

The histogram illustrates the deviation between actual and predicted IDR values. The highest concentration of data points is observed near the zero-error mark, indicating strong agreement between the model's predictions and the actual responses. Notably, approximately 95% of the data exhibit an error rate of less than 1%, underscoring the high accuracy and robustness of the ANFIS model in capturing the underlying structural behavior. These results confirm the model's effectiveness in forecasting IDR values across diverse geometric and material configurations, making it a reliable tool for seismic performance prediction in piloti-type structures.

Fig. 19 illustrates the performance evaluation of the ANFIS model based on eleven randomly selected test samples, which were excluded from the training process. The evaluation was conducted to validate the model's ability to generalize beyond the training data. The training and testing prediction curves exhibit a close match, indicating that the model successfully avoids overfitting, as evidenced by the absence of significant divergence between the two curves.

The predictive performance of the ANFIS model was further quantified using standard statistical metrics. The coefficient of determination (R^2) was calculated to be 0.967 for the training set, 0.942 for the test set, and 0.958 for the overall dataset, indicating excellent predictive accuracy and generalization capability.

In addition, the model's error metrics MAE, MSE, and $RMSE$ were found to be 0.017, 0.011, and 0.104, respectively. These results, summarized in Table 8, demonstrate the reliability and robustness of the ANFIS model in estimating the IDR under diverse input conditions.

Moreover, the parity plot presented in Fig. 19d confirms the high degree of alignment between the actual and predicted outputs, with minimal deviation. This indicates that the ANFIS model effectively captures underlying patterns in the data and is capable of anticipating structural responses with high accuracy, particularly in configurations expected to yield elevated IDR values.

4. Comparison for predicting seismic damage demand between ML models and FE model

FE models developed in LS-DYNA were applied to the piloti specimens described in Section 2.3, and the modeling details are illustrated in Fig. 20. Concrete components, including the foundation, beams, and columns, were discretized using eight-node solid elements (ELFORM = 1). Reinforcing bars were modeled with Hughes–Liu beam elements to accurately capture large deformation behavior. A refined mesh size of 25 mm was adopted in critical regions, while a coarser mesh of 50 mm was used in less sensitive areas to improve computational efficiency. The interaction between concrete and reinforcement was simulated using the CONSTRAINED_BEAM_IN_SOLID technique, ensuring displacement compatibility and realistic bond–slip behavior.

The constitutive behavior of concrete under monotonic and cyclic loading was modeled using the Concrete Damage Plasticity (CDP) model, which accounts for stiffness degradation and irreversible strains in tension and compression. Reinforcing steel

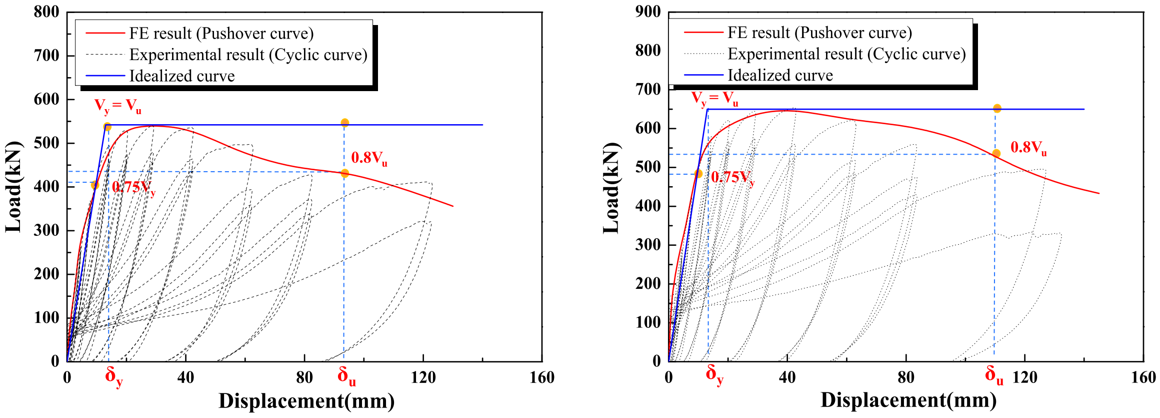

(a) Specimen 1

(b) Specimen 2

Fig. 21. Pushover results and idealized curves of piloti specimens.

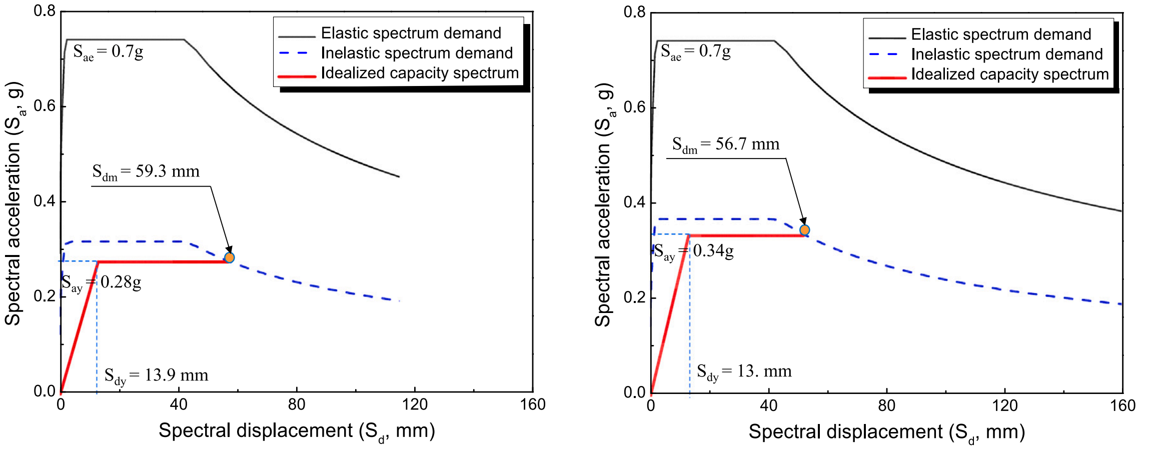

(a) Specimen 1

(b) Specimen 2

Fig. 22. Calculation of seismic demand (S_{dm}) using CSM.

was represented by the *MAT_PLASTIC_KINEMATIC model, incorporating isotropic and kinematic hardening to capture nonlinear behavior under cyclic loading.

The computation of the IDR was performed using the enhanced Capacity Spectrum Method (CSM), as described in Refs. [39–41], based on nonlinear pushover analysis. In the CSM procedure, the pushover curve, representing the relationship between base shear (V_{base}) and roof displacement (δ_{roof}), is transformed into an equivalent capacity spectrum in terms of spectral acceleration and spectral displacement for an idealized single-degree-of-freedom (SDOF) system, as illustrated in Fig. 21. The intersection of the capacity spectrum with the seismic demand spectrum defines the performance point, from which the displacement demand and corresponding IDR are obtained. In this study, the CSM-based IDR values derived from FE analyses are further used as benchmark results to validate the ML predictions, ensuring consistency between physics-based and data-driven approaches.

An elastic spectral acceleration (S_{ae}) of 0.7g was identified at the intersection point between the elastic response spectrum demand curve and the structure's elastic period. Based on this spectral acceleration, the spectral displacement demands (S_{dm}) were computed using relationships involving the elastic spectral acceleration (S_{ae}) and the yielding spectral acceleration (S_{ay}), in accordance with the CSM framework.

Subsequently, the maximum displacement demands (δ_m) at the roof level were estimated to be 59.3 mm for Specimen 1 and 56.7 mm for Specimen 2, as illustrated in Fig. 22. These displacement values correspond to the performance point on the capacity spectrum curve and represent the expected maximum deformation under seismic excitation.

Finally, IDR values were derived from the displacement demands, yielding 0.96% for Specimen 1 and 1.16% for Specimen 2. The slightly higher drift in Specimen 2 reflects its greater ductility and energy dissipation capacity, as observed in the nonlinear pushover response and confirmed through the spectral analysis.

Table 9
Comparison of predicted IDR values between FE model and ML model.

Specimen	Input parameter	Predicted IDR values (%)			Seismic performance level
		ML model	FE model	Difference (%)	
1	– $CN = 4$ – $CSR = 1.6$ – $WSR = 4.67$ – $f'_c = 21$ – $TS = 250$	1.62	1.77	8.33	Life safety (LS)
2	– $CN = 4$ – $CSR = 1.0$ – $WSR = 4.67$ – $f'_c = 21$ – $TS = 250$	1.34	1.48	9.45	Life safety (LS)

The best-fit model, identified as the ANFIS model, was utilized to predict the seismic performance of piloti structures in terms of IDR. The predicted IDR values were 0.88% for Specimen 1 and 1.05% for Specimen 2, respectively. These predictions were compared against the displacement-based IDR values obtained from nonlinear pushover analysis using FE simulations. The differences between the ANFIS-predicted values and those derived from the FE models were found to be 8.33% for Specimen 1 and 9.45% for Specimen 2, both of which fall below the commonly accepted threshold of 10% for model validation, as summarized in Table 9.

These results indicate that the ANFIS model exhibits high predictive accuracy and generalization capability, making it a reliable surrogate model for seismic performance estimation, particularly in preliminary design or assessment scenarios where computational efficiency is critical.

5. Predicting the optimal scheme of section shape ratios for seismic performance based on ML model

5.1. Predicting the optimal scheme of section shape ratios

The optimal constitutive scheme for piloti-type reinforced concrete structures in South Korea was identified using the ANFIS model, which demonstrated superior predictive accuracy across various configurations. Based on parametric variation of CSR and other input parameters, the model identified $WSR = 1.5$ as the most favorable WSR in terms of minimizing IDR and achieving high performance levels.

While Operational performance level can be achieved under multiple combinations of CSR and WSR, the machine learning-based results shown in Fig. 23 provide further insight into the relative robustness of different configurations. As shown, $WSR = 1.5$ consistently corresponds to lower and less dispersed IDR values across a wide range of CSR, indicating a more stable seismic response compared to higher WSR values. In contrast, larger WSR values exhibit increased dispersion in IDR, suggesting higher sensitivity to geometric variation. Therefore, $WSR = 1.5$ is identified as the most favorable configuration not only in terms of deformation control, but also in terms of performance stability, making it particularly suitable for design-oriented applications.

As illustrated in Fig. 23, piloti structures achieved an Operational performance level at both $WSR = 1.5$ and $WSR = 3.33$ when the CSR ranged from 1.0 to 1.5. Furthermore, Operational-level performance was observed at $WSR = 2.0$ when CSR increased from 1.5 to 2.25, and maintained at $WSR = 2.78$ when CSR exceeded 2.0 or was larger than 2.5. However, when CSR ranged between 1.5 and 2.5, piloti structures generally maintained an Immediate Occupancy (IO) performance level, regardless of the WSR value.

Based on these findings, the recommended optimal design scheme involves a CSR between 1.0 and 1.5, and a WSR between 1.5 and 2.78, which collectively ensure reliable seismic performance and minimize deformation demand in piloti structures. This guidance may serve as a practical reference for structural engineers during the design and retrofitting of mid-rise buildings in moderate to high seismic zones.

5.2. Recommendations for new design and retrofit applications

The results of this study offer practical guidance for both new structural design and the seismic retrofit of piloti-type reinforced concrete buildings in South Korea. The optimal ranges of column and WSR specifically, a CSR between 1.0 and 1.5, and a WSR between 1.5 and 2.78 were consistently associated with enhanced seismic performance, including lower IDR and favorable energy dissipation behavior.

Implications for new design: For newly constructed piloti-type buildings, it is recommended that structural engineers consider adopting the optimal CSR and WSR ranges identified in this study. These configurations promote balanced stiffness and ductility, ensuring that buildings meet or exceed performance objectives such as Operational or Immediate Occupancy levels under design-level earthquakes. Integrating these parameters into preliminary design decisions can streamline the development process and reduce the need for extensive nonlinear analyses.

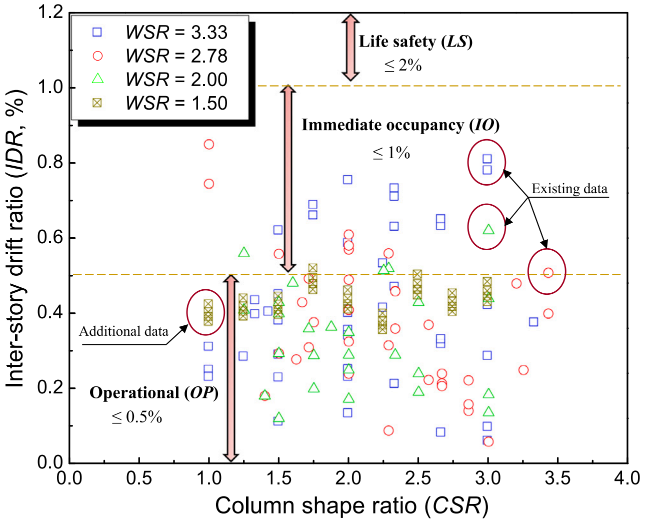

Fig. 23. Predicted the optimal scheme of section shape ratios-based ML model.

Table 10
Recommendations for new design and retrofit applications.

No.	Aspect	New design	Retrofit
1	CSR range	1.0–1.5	Adjust 1.0–1.5
2	WSR range	1.5–2.78	Adjust 1.5–2.78
3	Performance target	Operational (OP)	Operational (OP)
4	Design focus	Geometry optimization in early design phase	Enhance columns and add/modify walls
5	Application strategy	Apply optimal shape ratios in initial layout	Target critical zones for strengthening

Implications for retrofit design: For existing buildings requiring seismic upgrades, the findings offer a clear direction for improving performance through targeted geometric interventions. Retrofitting strategies may include: (1) Enlarging column cross-sections to bring CSR into the optimal range, (2) adding or thickening shear walls to adjust WSR and increase lateral resistance, and (3) reducing transverse spacing or redistributing vertical elements to improve global stiffness and minimize drift concentrations. The recommendations scheme of section shape ratios for new design and retrofit applications were shown in Table 10.

5.3. Recommendations based on seismic hazard levels

Given the variation in seismic hazard across regions in South Korea and other seismically active countries, it is essential to develop region-specific design strategies that account for local seismicity. Moderate seismic hazard zones are typically characterized by infrequent seismic events, where the return period for major earthquakes is relatively long and expected ground motions are moderate. In contrast, high seismic hazard zones are associated with more frequent or intense seismic activity, necessitating structural systems that can sustain higher acceleration levels and larger inelastic deformations.

Based on the results of the parametric analyses and ML-based predictions presented in this study, tailored recommendations have been developed for both moderate and high seismic hazard conditions. These recommendations primarily address optimal section shape ratios, namely the CSR and WSR, which were shown to significantly influence seismic performance in piloti-type RC structures.

A summary of the proposed design and retrofit schemes for each seismic hazard level categorized by application type, target performance level, and optimal shape ratio ranges is provided in Table 11.

6. Evaluation of the suggested optimal scheme-based ML through the FE model

The proposed optimal geometric scheme was applied to the piloti-type specimen described in Section 2.3, incorporating various shape ratio parameters, specifically the CSR and WSR. The evaluation covered a range of values, with CSR varying from 1.0 to 2.0 and WSR ranging from 1.5 to 3.5, as summarized in Table 12.

To verify the accuracy and feasibility of the ML-derived optimal scheme, a series of FE models were developed and subjected to nonlinear pushover analysis using LS-DYNA. The seismic performance of each configuration was assessed in terms of the IDR, following the methodology outlined in Section 4.

Table 11
Recommendations based on seismic hazard levels.

No.	Aspect	Moderate seismic hazard zones	High seismic hazard zones
1	CSR range	1.0–1.5 (preferred for maintaining drift control with reduced structural demand).	Narrowed to 1.0–1.3 to limit deformation concentration and enhance ductility in critical columns.
2	WSR range	1.5–2.78 (sufficient for lateral stiffness without overdesign).	2.0–2.78 (prioritizing walls with sufficient thickness for shear capacity and confinement).
3	Performance target	Immediate Occupancy (IO) level under design-level ground motions.	Operational (OP) level or higher, especially for essential facilities or post-earthquake functionality.
4	Design implication	Emphasis can be placed on balanced geometry, without necessarily increasing wall thickness or reinforcement to high levels. The use of ML-based predictive tools (e.g., ANFIS) is encouraged for preliminary design optimization.	Consider additional retrofitting elements such as boundary confinement zones, high-strength materials, or base isolation for critical infrastructure. Drift-sensitive systems should undergo stricter checks using nonlinear pushover or time–history analysis.
5	General note	Regardless of seismic zone, maintaining the optimal CSR–WSR ratios remains a critical indicator for reducing inter-story drift and avoiding soft-story collapse mechanisms in piloti-type structures.	

Table 12
Evaluation of the optimal scheme-based ML through FE models.

Column shape ratio (CSR)	Wall shape ratio (WSR)	Yielding spectral acceleration (S_{ay})	Spectral displacement demand (S_{dm})	Inter-story drift ratio (IDR)
1.0	1.5	0.266	32.11	1.529
1.2	1.5	0.270	31.91	1.520
1.5	1.5	0.278	31.76	1.512
1.8	1.5	0.262	34.67	1.651
2.0	1.5	0.262	34.71	1.653
1.0	2.0	0.285	31.28	1.490
1.2	2.0	0.307	31.19	1.485
1.5	2.0	0.313	30.61	1.458
1.8	2.0	0.284	33.23	1.582
2.0	2.0	0.282	33.53	1.597
1.0	2.5	0.292	31.19	1.485
1.2	2.5	0.315	30.02	1.429
1.5	2.5	0.320	29.55	1.407
1.8	2.5	0.291	32.45	1.545
2.0	2.5	0.289	32.75	1.560
1.0	2.8	0.293	31.05	1.479
1.2	2.8	0.315	30.41	1.448
1.5	2.8	0.322	29.61	1.410
1.8	2.8	0.292	32.37	1.541
2.0	2.8	0.289	32.67	1.555
1.0	3.5	0.279	35.12	1.672
1.2	3.5	0.292	33.52	1.596
1.5	3.5	0.299	32.76	1.560
1.8	3.5	0.300	32.62	1.553
2.0	3.5	0.303	32.30	1.538

The FE analysis results confirmed that the optimal scheme predicted by the ANFIS model aligns closely with the actual nonlinear response of the structures. In particular, the optimal performance range was achieved when CSR ranged from 1.0 to 1.5 and WSR was within 1.5 to 2.8, as illustrated in Fig. 24. Performance was most sensitive at $WSR = 1.5$ when CSR was between 1.0 and 1.5, and also at $WSR = 2.0$ when CSR exceeded 1.0. In contrast, when WSR increased from 2.5 to 2.8 while CSR remained between 1.0 and 1.5, the influence on performance became marginal, indicating a plateau in seismic improvement beyond a certain wall shape threshold. These findings reinforce the validity of the ML-based optimization and demonstrate that the derived optimal scheme is both practical and applicable across a range of realistic design configurations.

Fig. 25 presents the relative difference between IDR values predicted by the ANFIS-based ML model and those obtained from nonlinear pushover analysis using FE simulations. The heatmap is organized by varying combinations of CSR and WSR, which are critical geometric parameters influencing seismic response in piloti-type structures.

The results indicate that the largest discrepancies (up to 3.53%) occurred when $CSR = 1.0$ and $WSR = 1.5$, suggesting that the ML model is more sensitive to highly slender column configurations in combination with thinner wall systems. Conversely, minimal differences (<1.5%) were observed across a broad range of configurations, particularly when CSR values were between 1.5 and 2.0 and WSR ranged from 2.0 to 2.8.

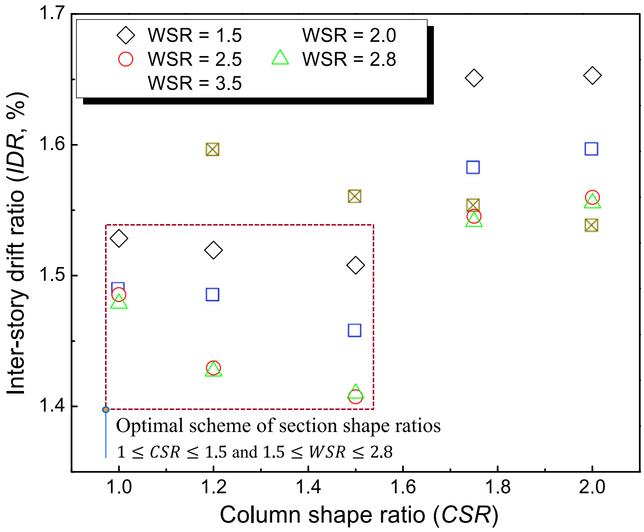

Fig. 24. Evaluation of the optimal scheme based on FE models.

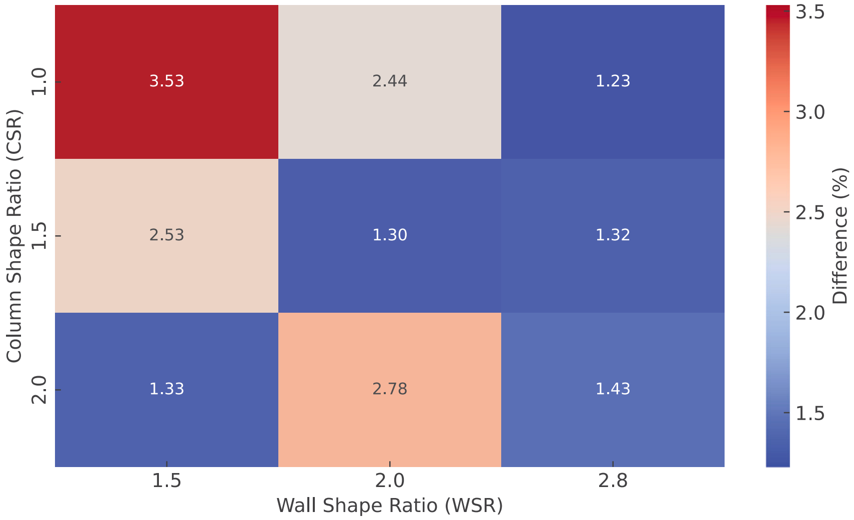

Fig. 25. Prediction differences between ML and FE.

These findings confirm that the ML model is most reliable within the identified optimal design zone, while prediction uncertainties increase near the geometric extremes. The figure thus serves as a useful diagnostic tool for identifying regions where ML models require additional calibration or should be supplemented with higher-fidelity simulation approaches.

7. Conclusions

Reliable and accurate prediction of seismic performance can significantly reduce the time and cost associated with structural analysis and decision-making. This study focuses on the application of ML techniques to predict the seismic behavior of piloti-type reinforced concrete structures. Two hybrid models were developed and evaluated for this purpose: the SVM and the ANFIS. Based on the comprehensive experimental, numerical, and data-driven investigations, the principal conclusions of this study are summarized as follows:

1. The CSR significantly influenced the performance of piloti structures, including strength capacity, damaged behavior, and energy dissipation. Rectangular columns have reduced resistance to bending or shear in the weak direction relative to square columns. The strength capacity increases by around 21%, while energy dissipation increases by 39.42%.

Table A.1
Statistics of dataset of piloti-type buildings in South Korea.

Case S#	Number of columns (CN)	Column section (CS)	Wall section (WS)	Column shape ratio (CSR)	Wall shape ratio (WSR)	Concrete compressive strength (f'_c)	Transverse spacing (TS)	Inter-story drift ratio (IDR)
1	7	300 × 800	500 × 180	2.67	2.78	17.31	300	0.209
2	7	300 × 800	500 × 180	2.67	2.78	17.87	300	0.214
3	8	300 × 700	500 × 180	2.33	2.78	18.22	200	0.207
4	8	300 × 700	500 × 180	2.33	2.78	22.49	200	0.460
5	8	300 × 700	500 × 180	2.33	2.78	22.13	200	0.459
6	11	400 × 600	500 × 180	1.50	2.78	17.99	200	0.294
7	5	350 × 600	500 × 180	1.71	2.78	17.73	250	0.493
8	5	400 × 1200	500 × 180	3.00	2.78	22.15	250	0.059
9	11	500 × 700	500 × 180	1.40	2.78	18.19	300	0.181
10	8	300 × 600	500 × 180	2.00	2.78	19.64	300	0.490
11	8	500 × 500	500 × 180	1.00	2.78	20.00	250	0.745
12	6	400 × 700	500 × 180	1.75	2.78	18.63	300	0.377
13	7	500 × 500	500 × 180	1.00	2.78	22.65	300	0.850
14	12	350 × 600	500 × 180	1.71	2.78	21.00	300	0.310
15	11	300 × 600	500 × 180	2.00	2.78	17.76	300	0.410
16	8	350 × 900	500 × 180	2.57	2.78	17.71	300	0.370
17	14	300 × 800	500 × 180	2.67	2.78	22.36	200	0.240
18	12	400 × 800	500 × 180	2.00	2.78	16.75	300	0.570
19	12	300 × 600	500 × 180	2.00	2.78	23.42	300	0.610
20	8	300 × 700	500 × 180	2.33	2.78	21.14	300	0.360
21	14	400 × 800	500 × 180	2.00	2.78	20.45	300	0.581
22	11	350 × 800	500 × 180	2.29	2.78	19.92	350	0.560
23	12	400 × 800	500 × 180	2.00	2.78	17.47	300	0.325
24	11	400 × 800	500 × 180	2.00	2.78	15.10	300	0.240
25	8	300 × 500	500 × 180	1.67	2.78	20.57	300	0.430
26	11	400 × 1300	500 × 180	3.25	2.78	17.25	200	0.250
27	8	800 × 250	500 × 180	3.20	2.78	19.54	250	0.480
28	12	400 × 600	500 × 180	1.50	2.78	17.24	200	0.559
29	2	350 × 1200	500 × 180	3.43	2.78	21.16	300	0.508
30	4	350 × 1200	500 × 180	3.43	2.78	22.02	300	0.400
31	10	350 × 800	500 × 180	2.29	2.78	18.52	200	0.088
32	8	350 × 1000	500 × 180	2.86	2.78	19.49	200	0.141
33	8	350 × 1000	500 × 180	2.86	2.78	18.94	200	0.159
34	8	350 × 1000	500 × 180	2.86	2.78	18.87	300	0.222
35	15	350 × 900	500 × 180	2.57	2.78	19.93	250	0.224
36	13	350 × 800	500 × 180	2.29	2.78	17.27	300	0.315
37	6	400 × 650	500 × 180	1.63	2.78	17.52	200	0.278
38	5	300 × 700	500 × 150	2.33	3.33	17.46	250	0.732
39	12	300 × 800	500 × 150	2.67	3.33	17.30	300	0.317
40	7	600 × 800	500 × 150	1.33	3.33	17.03	300	0.397
41	7	600 × 800	500 × 150	1.33	3.33	17.38	300	0.434
42	5	400 × 600	500 × 150	1.50	3.33	17.83	300	0.228
43	9	300 × 900	500 × 150	3.00	3.33	19.45	200	0.096
44	5	400 × 1200	500 × 150	3.00	3.33	22.15	250	0.059
45	4	300 × 600	500 × 150	2.00	3.33	16.91	200	0.355
46	8	400 × 800	500 × 150	2.00	3.33	23.37	300	0.754
47	7	300 × 800	500 × 150	2.67	3.33	18.41	300	0.632
48	11	400 × 600	500 × 150	1.50	3.33	18.86	300	0.620
49	10	400 × 600	500 × 150	1.50	3.33	16.43	250	0.110
50	11	300 × 600	500 × 150	2.00	3.33	17.76	300	0.410
51	8	400 × 700	500 × 150	1.75	3.33	21.30	300	0.660
52	13	400 × 400	500 × 150	1.00	3.33	18.74	300	0.310
53	7	300 × 800	500 × 150	2.67	3.33	24.09	300	0.081
54	10	400 × 500	500 × 150	1.25	3.33	18.20	300	0.283
55	12	400 × 800	500 × 150	2.00	3.33	22.18	300	0.408
56	12	400 × 800	500 × 150	2.00	3.33	21.25	300	0.586
57	6	400 × 700	500 × 150	1.75	3.33	21.37	300	0.688
58	7	400 × 900	500 × 150	2.25	3.33	21.90	300	0.414
59	10	400 × 900	500 × 150	2.25	3.33	20.24	300	0.532
60	10	300 × 600	500 × 150	2.00	3.33	25.60	300	0.400
61	14	350 × 500	500 × 150	1.43	3.33	16.60	250	0.404
62	9	300 × 600	500 × 150	2.00	3.33	21.77	300	0.409
63	10	300 × 600	500 × 150	2.00	3.33	21.63	300	0.132
64	16	400 × 600	500 × 150	1.50	3.33	18.11	300	0.289

(*continued on next page*)

Table A.1 (*continued*).

65	12	300 × 900	500 × 150	3.00	3.33	19.25	250	0.285
66	16	300 × 900	500 × 150	3.00	3.33	19.51	250	0.422
67	13	300 × 600	500 × 150	2.00	3.33	19.83	300	0.247
68	10	400 × 400	500 × 150	1.00	3.33	17.21	300	0.248
69	9	300 × 900	500 × 150	3.00	3.33	15.65	300	0.780
70	18	300 × 600	500 × 150	2.00	3.33	24.29	300	0.230
71	12	400 × 600	500 × 150	1.50	3.33	17.82	300	0.440
72	12	300 × 700	500 × 150	2.33	3.33	15.93	300	0.470
73	13	400 × 400	500 × 150	1.00	3.33	20.42	300	0.230
74	12	400 × 600	500 × 150	1.50	3.33	24.04	300	0.450
75	9	300 × 700	500 × 150	2.33	3.33	21.06	300	0.630
76	8	300 × 700	500 × 150	2.33	3.33	23.11	300	0.710
77	12	400 × 800	500 × 150	2.00	3.33	15.49	300	0.340
78	17	400 × 600	500 × 150	1.50	3.33	16.94	300	0.380
79	14	300 × 800	500 × 150	2.67	3.33	16.39	300	0.650
80	13	400 × 800	500 × 150	2.67	3.33	17.68	300	0.330
81	12	300 × 1000	500 × 150	3.33	3.33	19.99	300	0.375
82	12	400 × 1200	500 × 150	3.00	3.33	16.48	300	0.810
83	15	400 × 800	500 × 150	2.00	3.33	20.29	300	0.250
84	13	500 × 1000	500 × 150	2.00	3.33	15.87	300	0.460
85	10	300 × 700	500 × 150	2.33	3.33	18.95	300	0.211
86	11	400 × 600	500 × 250	1.50	2.00	17.99	200	0.294
87	11	500 × 700	500 × 250	1.40	2.00	18.19	300	0.181
88	8	400 × 800	500 × 250	2.00	2.00	17.63	300	0.250
89	10	400 × 800	500 × 250	2.00	2.00	19.35	300	0.290
90	8	350 × 800	500 × 250	2.29	2.00	23.28	300	0.520
91	8	400 × 900	500 × 250	2.25	2.00	23.74	300	0.514
92	12	300 × 600	500 × 250	2.00	2.00	25.08	300	0.173
93	12	300 × 600	500 × 250	2.00	2.00	19.01	300	0.185
94	17	400 × 500	500 × 250	1.25	2.00	24.61	200	0.410
95	12	300 × 900	500 × 250	3.00	2.00	18.50	300	0.621
96	13	400 × 750	500 × 250	1.88	2.00	18.92	200	0.364
97	8	400 × 700	500 × 250	1.75	2.00	18.40	250	0.289
98	15	400 × 600	500 × 250	1.50	2.00	17.17	300	0.121
99	11	300 × 900	500 × 250	3.00	2.00	18.78	300	0.136
100	11	400 × 1000	500 × 250	2.50	2.00	16.36	300	0.191
101	11	400 × 1000	500 × 250	2.50	2.00	18.26	300	0.240
102	18	400 × 700	500 × 250	1.75	2.00	22.22	300	0.200
103	12	350 × 600	500 × 250	1.71	2.00	20.42	200	0.360
104	11	300 × 600	500 × 250	2.00	2.00	25.23	300	0.350
105	18	400 × 500	500 × 250	1.25	2.00	18.17	300	0.560
106	15	300 × 700	500 × 250	2.33	2.00	18.89	300	0.290
107	8	400 × 600	500 × 250	1.50	2.00	19.26	200	0.400
108	17	400 × 600	500 × 250	1.50	2.00	16.61	300	0.430
109	10	400 × 1200	500 × 250	3.00	2.00	14.86	300	0.440
110	11	400 × 1000	500 × 250	2.50	2.00	24.67	300	0.430
111	10	500 × 800	500 × 250	1.60	2.00	21.77	300	0.482

2. This study developed a data-driven framework to predict the seismic deformation demand of piloti-type reinforced concrete buildings using ML techniques. Based on 111 structural configurations, CSR and WSR were identified as dominant parameters governing inter-story drift behavior. Among the evaluated models, the ANFIS approach demonstrated superior predictive accuracy, with R^2 values exceeding 0.95, and was validated through experimental results and FE analyses. The proposed framework provides practical guidance for performance-based seismic assessment and retrofit decision-making.
3. FE simulations using LS-DYNA were conducted to validate the ML predictions through pushover analysis. The predicted and simulated IDR showed strong agreement, with discrepancies remaining below 10%. Parametric analyses further identified optimal seismic performance within a CSR range of 1.0–1.5 and a WSR range of 1.5–2.78, highlighting the critical role of section shape ratios in controlling seismic deformation.
4. Based on these findings, design recommendations were proposed for both new construction and seismic retrofit scenarios. The recommendations were further tailored to regional seismic hazard levels, distinguishing between moderate and high seismic risk zones. The resulting design matrix provides a practical reference for engineers, enabling them to select optimal CSR–WSR configurations that ensure target performance levels such as Immediate Occupancy or Operational condition.
5. The integration of ML into performance-based seismic design offers a powerful tool for efficient, reliable, and data-informed decision-making. The proposed framework has the potential to complement conventional analysis methods, reduce computational burden, and enhance the resilience of RC piloti structures in seismically active regions.
6. While the present study adopts a simplified set of geometric and material parameters for a design-oriented, data-driven comparison of seismic performance in piloti-type RC buildings, the authors acknowledge that incorporating additional global structural descriptors may further enhance predictive capability. In addition, the experimental and numerical investigations

are limited to two representative specimens intended for mechanistic validation rather than exhaustive statistical verification. Accordingly, future work should expand the dataset, integrate time–history analysis for dynamic validation, and include broader experimental verification to further support performance-based seismic design and retrofit decision-making.

CRediT authorship contribution statement

Quoc Bao To: Writing – review & editing, Writing – original draft, Validation, Software, Methodology, Investigation, Formal analysis, Conceptualization. **Gayoon Lee:** Writing – review & editing, Formal analysis. **Jiuk Shin:** Writing – review & editing, Formal analysis. **L. Minh Dang:** Writing – review & editing, Investigation. **Sang Whan Han:** Writing – review & editing, Investigation. **Kihak Lee:** Writing – review & editing, Supervision, Resources, Project administration, Formal analysis.

Declaration of competing interest

The authors declare that they have no known competing financial interests or personal relationships that could have appeared to influence the work reported in this paper.

Acknowledgments

This research was supported by Basic Science Research Program through the National Research Foundation of Korea (NRF) funded by the Ministry of Education, Republic of Korea (RS-2024-00461244).

Appendix

See Table A.1.

Data availability

The authors do not have permission to share data.

References

[1] Q.B. To, J. Shin, G. Lee, H. An, K. Lee, Experimental assessment and effective bond length for rc columns strengthened with aramid frp sheets under cyclic loading, Eng. Struct. 294 (2023) 116642.
[2] Q.B. To, K. Lee, S.J. Kim, J. Shin, Quantifying effect of post-tensioned bars for precast concrete shear walls, Sustainability 14 (10) (2022) 6141.
[3] Q.B. To, J. Shin, S.M. Kang, T. Ahn, C. Jeong, K. Lee, Analytical and experimental investigation on performance of enta damper systems for rc moment frame under cyclic loading, Eng. Struct. 314 (2024) 118386.
[4] Q.B. To, J. Shin, J. Kim, S.W. Han, K. Lee, Finite element analysis-based blast and seismic performance evaluation for rc frame with retrofitted enta damper systems, Eng. Struct. 313 (2024) 118300.
[5] H.S. Lee, D.W. Ko, Shaking table tests of a high-rise rc bearing-wall structure with bottom piloti stories, J. Asian Archit. Build. Eng. 1 (1) (2002) 47–54.
[6] H.S. Lee, D.W. Ko, Seismic response characteristics of high-rise rc wall buildings having different irregularities in lower stories, Eng. Struct. 29 (11) (2007) 3149–3167.
[7] Q.B. To, G. Lee, H. An, D. Lee, D.H. Lee, K. Lee, Experimental and numerical evaluation of afrp-retrofitted reinforced concrete piloti structures: Hysteretic behavior, plastic hinge modeling, and optimal retrofitting, J. Build. Eng. (2025) 113790.
[8] J. Tanjung, Y. Sanada, F. Nugroho, S. Wardi, et al., Seismic analysis of damaged buildings based on postearthquake investigation of the 2018 palu earthquake, GEOMATE J. 18 (70) (2020) 116–122.
[9] A.G. Sextos, E.I. Katsanos, G.D. Manolis, Ec8-based earthquake record selection procedure evaluation: Validation study based on observed damage of an irregular r/c building, Soil Dyn. Earthq. Eng. 31 (4) (2011) 583–597.
[10] J. Shin, K. Lee, S.H. Jeong, H.S. Lee, J. Kim, Experimental and analytical studies on buckling-restrained knee bracing systems with channel sections, Int. J. Steel Struct. 12 (2012) 93–106.
[11] S.V. Committee, et al., Performance-Based Seismic Engineering, Structural Engineers Association of California, Sacramento, California, 1995.
[12] FEMA 349, Action Plan for Performance – Based Seismic Design, vol. 7, Federal Emergency Management Agency, Washington, DC, 2000, (2).
[13] Eurocode 8, Design of Structures for Earthquake Resistance-Part 1: General Rules, Seismic Actions and Rules for Buildings, vol. 10, European Committee for Standardization, Brussels, 2005.
[14] A. Ghobarah, Performance-based design in earthquake engineering: State of development, Eng. Struct. 23 (8) (2001) 878–884.
[15] Q.B. To, K.V.A. Pham, G. Lee, M. Shin, D.W. Shin, K. Lee, Experimental and fem evaluation of the influence of interlayer bonding strength in 3d printed concrete members under compressive and flexural loadings, J. Build. Eng. 94 (2024) 109979.
[16] BSSC (US), A.T. Council, NEHRP Guidelines for the Seismic Rehabilitation of Buildings, vol. 1, Federal Emergency Management Agency, 1997.
[17] FEMA 356, Prestandard and Commentary for the Seismic Rehabilitation of Buildings, vol. 7, Federal Emergency Management Agency, Washington, DC, 2000, (2).
[18] F. Kazemi, N. Asgarkhani, R. Jankowski, Machine learning-based seismic response and performance assessment of reinforced concrete buildings, Arch. Civ. Mech. Eng. 23 (2) (2023) 94.
[19] C. Cosgun, Machine learning for the prediction of evaluation of existing reinforced concrete structures performance against earthquakes, in: Structures, vol. 50, Elsevier, 2023, pp. 1994–2003.
[20] Q.B. To, G. Lee, J. Shin, N.H. Cuong, K. Lee, Cost-efficient seismic retrofit strategy for afrp-retrofitted rc piloti frames using ml-driven plastic hinge modeling, Compos. Struct. (2025) 119962.
[21] Q.B. To, K. Lee, N.H. Cuong, J. Shin, Development of machine learning based seismic retrofit scheme for afrp retrofitted rc column, in: Structures, vol. 69, Elsevier, 2024, 107279.

[22] D.A. Skolnik, J.W. Wallace, Critical assessment of interstory drift measurements, J. Struct. Eng. 136 (12) (2010) 1574–1584.

[23] E. Yu, D. Skolnik, D.H. Whang, J.W. Wallace, Forced vibration testing of a four-story reinforced concrete building utilizing the nees@ ucla mobile field laboratory, Earthq. Spectra 24 (4) (2008) 969–995.

[24] M. Celebi, A. Sanli, Gps in pioneering dynamic monitoring of long-period structures, Earthq. Spectra 18 (1) (2002) 47–61.

[25] A.M. Wahbeh, J.P. Caffrey, S.F. Masri, A vision-based approach for the direct measurement of displacements in vibrating systems, Smart Mater. Struct. 12 (5) (2003) 785.

[26] G. Fu, A.G. Moosa, An optical approach to structural displacement measurement and its application, J. Eng. Mech. 128 (5) (2002) 511–520.

[27] STC01015, Structural Design Criteria, Process Industry Practices, Austin, TX, USA, 2007.

[28] P. Mohurd, JGJ 3-2010 technical specification for concrete structures of tall building, 2010.

[29] I. Shakir, M.A. Jasim, S.S. Weli, High rise buildings: Design, analysis, and safety: An overview, Int. J. Archit. Eng. Technol. 8 (2021) 1–13.

[30] V. Vapnik, The Nature of Statistical Learning Theory, Springer science & business media, 2013.

[31] Q.B. To, J. Shin, D.H. Lee, S. Woo, K. Lee, Parametric optimization and cost-efficient prediction of blast retrofit for afrp-retrofitted rc columns using ml-driven finite element modeling, Compos. Struct. (2025) 119498.

[32] V. Vapnik, S. Golowich, A. Smola, Support vector method for function approximation, regression estimation and signal processing, Adv. Neural Inf. Process. Syst. 9 (1996).

[33] R. Collobert, S. Bengio, Svmtorch: Support vector machines for large-scale regression problems, J. Mach. Learn. Res. 1 (Feb) (2001) 143–160.

[34] N. Cristianini, J. Shawe-Taylor, An Introduction To Support Vector Machines and Other Kernel-Based Learning Methods, Cambridge University Press, 2000.

[35] J.S. Jang, Anfis: Adaptive-network-based fuzzy inference system, IEEE Trans. Syst. Man Cybern. 23 (3) (1993) 665–685.

[36] S. Prakash, S.K. Sinha, Automatic load frequency control of six areas' hybrid multi-generation power systems using neuro-fuzzy intelligent controller, IETE J. Res. 64 (4) (2018) 471–481.

[37] P.A. Sari, M. Suhatril, N. Osman, M.A. Mu'azu, J. Katebi, A. Abavisani, N. Ghaffari, E. Sadeghi Chahnasir, K. Wakil, M. Khorami, et al., Developing a hybrid adoptive neuro-fuzzy inference system in predicting safety of factors of slopes subjected to surface eco-protection techniques, Eng. Comput. 36 (2020) 1347–1354.

[38] A. Talei, L.H.C. Chua, C. Quek, P.E. Jansson, Runoff forecasting using a Takagi–Sugeno neuro-fuzzy model with online learning, J. Hydrol. 488 (2013) 17–32.

[39] P. Fajfar, A nonlinear analysis method for performance-based seismic design, Earthq. Spectra 16 (3) (2000) 573–592.

[40] A.K. Chopra, R.K. Goel, Capacity-demand-diagram methods based on inelastic design spectrum, Earthq. Spectra 15 (4) (1999) 637–656.

[41] E. Miranda, Estimation of inelastic deformation demands of sdof systems, J. Struct. Eng. 127 (9) (2001) 1005–1012.